



Journal Article

Uncertainties related to the representation of momentum transport in shallow convection

Author(s):

Schlemmer, Linda; Bechtold, P.; Sandu, I.; Ahlgrim, M.

Publication Date:

2017-06

Permanent Link:

<https://doi.org/10.3929/ethz-b-000190715> →

Originally published in:

Journal of Advances in Modeling Earth Systems 9(2), <http://doi.org/10.1002/2017MS000915> →

Rights / License:

[Creative Commons Attribution-NonCommercial-NoDerivatives 4.0 International](#) →




This page was generated automatically upon download from the [ETH Zurich Research Collection](#). For more information please consult the [Terms of use](#).



RESEARCH ARTICLE

10.1002/2017MS000915

Uncertainties related to the representation of momentum transport in shallow convection

L. Schlemmer^{1,2} , P. Bechtold², I. Sandu² , and M. Ahlgrimm² 

¹ETH Zurich, Institute for Atmospheric and Climate Science, Zurich, Switzerland, ²European Centre for Medium-Range Weather Forecasts, Reading, UK

Key Points:

- Convective momentum transport in LES data and a bulk mass-flux parametrization is analyzed
- Convective mass flux and entrainment/detrainment are well represented by the parametrization, in-cloud values for momentum are challenging
- Uncertainties related to convective momentum transport as represented by an SPP approach are compared to convective variability within the LES

Correspondence to:

L. Schlemmer,
linda.schlemmer@alumni.ethz.ch

Citation:

Schlemmer, L., P. Bechtold, I. Sandu, and M. Ahlgrimm (2017), Uncertainties related to the representation of momentum transport in shallow convection, *J. Adv. Model. Earth Syst.*, *9*, 1269–1291, doi:10.1002/2017MS000915.

Received 9 JAN 2017

Accepted 6 APR 2017

Accepted article online 14 APR 2017

Published online 25 MAY 2017

© 2017. The Authors.

This is an open access article under the terms of the Creative Commons Attribution-NonCommercial-NoDerivs License, which permits use and distribution in any medium, provided the original work is properly cited, the use is non-commercial and no modifications or adaptations are made.

Abstract Convective momentum transport (CMT) has mostly been studied for deep convection, whereas little is known about its characteristics and importance in shallow convection. In this study, CMT by shallow convection is investigated by analyzing both data from large-eddy simulations (LESs) and reforecasts performed with the Integrated Forecasting System (IFS) of the European Centre for Medium-Range Weather Forecasts (ECMWF). In addition, the central terms underlying the bulk mass-flux parametrization of CMT are evaluated offline. Further, the uncertainties related to the representation of CMT are explored by running the stochastically perturbed parametrizations (SPP) approach of the IFS. The analyzed cases exhibit shallow convective clouds developing within considerable low-level wind shear. Analysis of the momentum fluxes in the LES data reveals significant momentum transport by the convection in both cases, which is directed downgradient despite substantial organization of the cloud field. A detailed inspection of the convection parametrization reveals a very good representation of the entrainment and detrainment rates and an appropriate representation of the convective mass and momentum fluxes. To determine the correct values of mass-flux and in-cloud momentum at the cloud base in the parametrization yet remains challenging. The spread in convection-related quantities generated by the SPP is reasonable and addresses many of the identified uncertainties.

1. Introduction

Cumulus convection transports heat and moisture as well as momentum upward and downward. Especially in flows that exhibit strong vertical wind shear such as the trade wind region the vertical displacement of air with differential horizontal momentum from lower to upper levels is a crucial process that contributes to the overall momentum budget. Carr and Bretherton [2001] have investigated convective momentum transport (CMT) as deduced from the momentum budget residual in reanalysis data. They found a significant contribution with accelerations up to $2 \text{ m s}^{-1} \text{ d}^{-1}$ from the residual to the budget below 850 hPa, speculating that this transport results from momentum transport by shallow convection. The budget residual for the Tropical Ocean and Global Atmosphere Coupled Ocean-Atmosphere Response Experiment (TOGA-COARE) intense observing period showed a link between deep cumulus convection and the acceleration-deceleration of the large-scale horizontal motion [Tung and Yanai, 2002a, 2002b]. The associated CMT was modulated by various atmospheric disturbances. Moreover, they identified that CMT may either be upgradient or downgradient, depending on the organization of convection. For unorganized convection, CMT tends to be downgradient, meaning that it decreases the wind shear. For organized convective systems, CMT can become upgradient and accelerate the mean flow, which has especially been documented for the line-normal direction in squall lines [LeMone, 1983]. In addition, CMT regulates near-surface wind speed and the associated surface wind stress. Thus, it crucially impacts the coupling between the atmosphere and the ocean [Chelton et al., 2001]. Moreover, CMT can influence the central pressure and track of tropical cyclones [Hogan and Pauley, 2007].

Recognizing the importance of CMT by both shallow and deep convection for the climate, a fair amount of work has been devoted to include CMT into parametrization schemes for convection within the mass-flux framework [e.g., Schneider and Lindzen, 1976; Kershaw and Gregory, 1997; Gregory et al., 1997; Gregory and Miller, 1989] or using superparametrization approaches [e.g., Cheng and Xu, 2014; Tulich, 2015]. Zhang and McFarlane [1995], Inness and Gregory [1997], and Wu et al. [2007] demonstrated that the mean climate in global climate simulations critically depends on the inclusion of CMT. Moreover, it was shown that the biases in the surface winds could be reduced with the inclusion of a CMT parametrization [Richter and Rasch,

2008]. The parametrizations for CMT have however originally been developed based on the transport of scalar quantities, such as moisture and temperature, while the transport of momentum has generally received less attention. Yet the transport of momentum differs from the transport of moisture or heat. As the atmosphere becomes more unstable and convective transport is driven by plumes instead of vortices, the momentum transport within the surface layer becomes increasingly inefficient, in contrast to scalar transport [Li and Bou-Zeid, 2011]. Thus, the applicability of the mass-flux approximation to CMT has recently been questioned [Zhu, 2015]. A further critical aspect in the parametrization of CMT is the treatment of the pressure gradient [Zhang and Cho, 1991]. The in-cloud horizontal winds are affected by the horizontal pressure gradient across the updraft, which accelerates the in-cloud winds [see e.g., Kershaw and Gregory, 1997].

While convective momentum transport and its parametrization has been studied a fair amount for deep convection [see e.g., Grubišić and Moncrieff, 2000; Zhang and Wu, 2003], little is documented about its importance in shallow convection, and its representation in parametrization schemes for shallow convection. It is not clear, how well parametrizations capture both the uncertainties concerning the representation of the pressure gradient across updrafts and the decline in the efficiency of momentum transport with increasing instability. In contrast to deep convection, which is partly resolved, shallow convection shows considerably less organization and remains a subgrid scale process, even in present-day resolutions of Numerical Weather Prediction (NWP) models of $\mathcal{O}(10\text{ km})$. Brown [1999] used large-eddy simulations (LESs) to investigate the influence of shear on CMT in shallow convection for cases of downgradient transport. He demonstrated that the cross-cloud pressure gradient is a dominant term in the in-cloud momentum budget, even for shallow convection.

In this study, we take advantage of LES of shallow convection on large domains which have become available in the last years thanks to the increased computer power. Thereby we follow on the Brown [1999] study and explore more in depth the characteristics of CMT for a case of trade wind cumulus where clouds organize strongly, and an extratropical cold-air outbreak case, that is characterized by strong baroclinicity. First, the LES data are used to explore the momentum fluxes in the two cases across different states of organization of the cloud field. The focus lies on the question as to whether the momentum flux depends on the organization of the cloud field. Second, the LES data are used to explore in more detail the idea raised in Zhu [2015], that although the bulk mass-flux approach is widely used for shallow convection it may not be entirely suitable to represent vertical transport. More specifically, we use the LES data to investigate whether the LES-derived CMT characteristics can be reproduced by applying the mass-flux approximation to CMT. We also search to understand the shortcomings of the different assumptions underlying this approach, by taking a close look at the shallow convection parametrization scheme used in the Integrated Forecast System (IFS) of the European Centre for Medium-Range Weather Forecasts (ECMWF) [Bechtold et al., 2014] as a typical example of a bulk mass-flux parameterization for shallow convection. The initial part of this analysis relies entirely on LES output, with the IFS merely providing an example of how mass-flux transport is approximated in a shallow convection parameterization. Further along, we will also compare LES and IFS results directly. A limitation here is that the idealized forcing used for the LES does not exactly match the forcing in the IFS. It might seem more prudent to rely on the more conventional approach of using equally forced single column model experiments for comparison with LES. However, these cannot always capture the parameterization response in the fully interactive 3-D model adequately, which may be particularly relevant for momentum transport. Thus, we attempt the direct comparison with the fully interactive global model, but a degree of caution is required when interpreting results. Finally, we try to address a different aspect of uncertainty unrelated to the initial forcing, namely the part related to parameter uncertainty in the shallow convection scheme.

A common approach to deal with model uncertainties and to indicate the probability of an event is to employ ensemble forecasts [e.g., Leutbecher and Palmer, 2008]. In addition to the perturbations applied to the initial conditions, the schemes representing unresolved physical processes are stochastically perturbed. The uncertainties stemming from an imperfect representation of physical processes within parametrization schemes can be considered by sampling chosen parameters between ensemble members [e.g., Bowler et al., 2008; Baker et al., 2014; McCabe et al., 2016]. At the European Centre for Medium-Range Weather Forecasts (ECMWF), currently two different approaches are being pursued: the perturbations can be applied either to the tendencies from the routines (stochastically perturbed parametrization tendencies, SPPT) [Buizza et al., 1999] or by directly perturbing parameters within the parametrizations (stochastically

perturbed parametrizations, SPP) [Ollinaho *et al.*, 2016; Leutbecher *et al.*, 2016]. Here we follow the latter approach and investigate how much of the uncertainty underlying the parametrization of CMT by shallow convection can be captured by stochastically perturbing key parameters.

First, the two cases, the LES runs and the IFS short-range reforecasts are described (section 2). A general overview over the LES and IFS results is given in section 3. In section 4, the LES output is used to scrutinize the applicability of the mass-flux approximation and its underlying assumptions to CMT. Then, in section 5, the momentum fluxes and the assumptions underlying their parametrization are analyzed and compared between the IFS and the LES data. Section 6 reviews the uncertainties underlying CMT and investigates to what extent the SPP approach captures these uncertainties. A discussion and conclusion of the results is given in section 7.

2. Setup

2.1. RICO

The first case is based on the RICO (Rain in Cumulus over the Ocean) study [Rauber *et al.*, 2007]. The LES data set used is documented in Seifert *et al.* [2015]. The setup follows the GEWEX Cloud System Study (GCSS) RICO model intercomparison study [vanZanten *et al.*, 2011]. Simulations were performed using the University of California, Los Angeles (UCLA) large-eddy simulation (LES) model [see Stevens *et al.*, 2005]. The UCLA-LES solves the three-dimensional Ogura-Phillips anelastic equations, where one assumes an isentropic background state. The prognostic variables are the three components of the wind velocity (u , v , and w), the total water mixing ratio q_t , the liquid water potential temperature θ_l , and the microphysical species. The UCLA-LES uses a third-order Runge-Kutta scheme for the time integration, a fourth-order-centered scheme for the advection of momentum and a flux-limited fourth-order upwind scheme for the advection of scalars. A Smagorinsky-type scheme is employed to represent subgrid scale (sgs) mixing. Surface fluxes of heat and moisture are calculated employing similarity theory given a fixed sea-surface temperature. Cloud microphysical processes are parametrized based on the two-moment warm rain scheme of Seifert and Beheng [2001] with some simplifications and refinements detailed in Stevens and Seifert [2008].

The LES domain contains $2048 \times 2048 \times 200$ grid points, to span a simulated volume of $51.2 \text{ km} \times 51.2 \text{ km} \times 5 \text{ km}$. The grid is isotropic with a grid spacing of $\Delta x = 25 \text{ m}$ and has double periodic lateral boundary conditions. We use their "rico, N070" simulation. These data represent a case of shallow trade wind cumuli. The peculiarity of the simulations lies in the organization of the shallow convection from random clouds into larger systems during the course of the simulation [see e.g., Seifert *et al.*, 2015, Figure 2]. It is thus useful for studying CMT across different organization states of shallow convection. We pick two selected time steps for our analysis, namely 10 (unorganized state), and 60 h (organized state) into the simulation to sample different states of organization. The exceptionally large domain and multitude of simulated clouds yield a large sample for the analysis.

To analyze the representation of CMT in the IFS, short-range reforecasts (48 h) have been performed using version CY43R1 (operational since November 2016) at a resolution of approximately 16 km at the equator (spectral truncation 639 cubic octahedral grid) and a vertical resolution of 137 levels. The short-range reforecasts are initialized from the ERA INTERIM reanalysis [Dee *et al.*, 2011], at 00 UTC each other day between 16 December 2004, 00 UTC to 28 December 2004, which covers large parts of the undisturbed period of the RICO campaign. As the LES data are based on the idealized case, the meridional wind profile differed considerably between the LES data and the ERA INTERIM initial conditions. In order to obtain a better match between the IFS and LES, meridional winds are nudged toward the prescribed wind of -3.8 m s^{-1} of the GCSS study in a domain covering $500 \times 500 \text{ km}$ with a time scale of 6 h in the IFS. Apart from this local nudging, the IFS runs freely.

As mentioned in section 1, a closer agreement between the LES and IFS forcings would be desirable to enable a better direct comparison between simulation and forecast results. As we were limited to using existing LES results here, the cases discussed are a compromise.

2.2. CONSTRAIN

The setup for the cold-air outbreak follows the case study described in Field *et al.* [2014]. It is based on observations taken during the Met Office CONSTRAIN campaign and associated NWP runs using a

horizontal grid spacing of 1 km. Observations show that this day was characterized by northerly flow and stratocumulus clouds at 66°N–11°W. As cold air is advected over warmer sea, the stratocumulus transitions to mixed-phase cumulus clouds at around 60°N, prior to reaching land. Moreover, the flow shows a strong northerly component with significant wind shear indicating a highly baroclinic situation. Cold-air outbreaks occur frequently [Brümmer and Pohlmann, 2000] and influence the air-sea exchange of momentum, heat, and moisture considerably [e.g., Nowlin and Parker, 1974].

LESs are performed using the UCLA-LES [see Tomassini *et al.*, 2017]. (The setup and the forcing data for the LES are documented at http://appconv.metoffice.com/cold_air_outbreak/constrain_case/crm_setup.html.) In contrast to the RICO simulations, a two-moment ice-microphysics scheme including ice, snow, graupel, and hail as cold species developed by Seifert and Beheng [2006] is used. Radiative fluxes are calculated interactively using the “correlated- k ” method in combination with a δ -four stream method [Fu and Liou, 1993; Pincus and Stevens, 2009]. The simulation uses a grid spacing of $\Delta x = 250$ m in the horizontal and a stretched grid in the vertical with a minimum grid spacing of $\Delta z = 25$ m. The domain spans 96×96 km² in the horizontal and 168 levels up to 4980 m in the vertical. The roughness length for momentum is set to 6.6×10^{-4} m and the roughness length for scalars to 3.7×10^{-6} m. A time-varying sea-surface temperature (SST) is prescribed to mimic the southward advection of the domain. In contrast to the setup proposed in Field *et al.* [2014], the initial values of u and v are used as the geostrophic winds u_g and v_g , respectively. The simulation is run for 14.5 h. The first 1.5 h are considered as spin-up period.

IFS reforecasts for the CONSTRAIN case are started from the operational analysis and run for 36 h over the period 30 January 2010, 12 UTC to 1 February 2010, 00 UTC. As for the RICO case, IFS version CY43R1 at a resolution of approximately 16 km at the equator and a vertical resolution of 137 levels is used.

For the comparison of the IFS with the LES, a domain that follows the LES track moving southward is extracted from the global IFS data for the CONSTRAIN case. It covers an area of $1^\circ \times 1^\circ$ and its center point is located at 66°N, 11°W at 00 UTC on 31 January 2010. The domain is moved at a constant speed to 60°N, 8.7°W at 13 UTC on 31 January 2010.

2.3. Stochastically Perturbed Parametrizations (SPP)

The current implementation of SPP allows simultaneous perturbations of up to 20 parameters and variables. The 20 parameters and variables have been selected as these variables are known to carry a large uncertainty in the parametrization schemes, plus they play an important role within the parametrization. More details on the SPP can be found in Ollinaho *et al.* [2016]. Concerning CMT the processes underlying the convection (entrainment/detrainment, the autoconversion of convective cloud condensate, and the CAPE adjustment scale for deep convection only) as well as the convective momentum tendency itself (currently only active for cloud depths in excess of 200 hPa) accounting for upgradient momentum transport in 10% of the cases are perturbed within the IFS SPP approach. For the current study, we restrict the perturbations to those parameters that directly affect the parametrization of convection. For the short-period CONSTRAIN case, we create 25 members. For the longer-period RICO case, 16 members are created and the 14 simulation days are treated as individual members, resulting in $16 \times 14 = 224$ members of daily-averaged values. The individual members all start from the same initial conditions, both in RICO and CONSTRAIN. The sampling in time in the RICO case means that the initial conditions are varied between the 14 individual days.

In order to estimate the variability within the LES data, we subdivide the LES domain into n equally large subdomains and average the variables over these subdomains [cf., Shutts and Palmer, 2007]. We have set n to 16, such that each subdomain in RICO covers 512×512 grid points (12.8 km \times 12.8 km) for the RICO case and 96×96 grid points (24 km \times 24 km) for the CONSTRAIN case.

Strictly speaking, the subsampling of the LES data, which is a sampling in space does not correspond to the variability given by the SPP, which is a sampling in parameter space. Yet it gives us an opportunity to explore the uncertainty connected to CMT.

A full discussion on spread and uncertainty will be provided near the end of this article in section 6. However, spread in the form of the interquartile range over the set of realizations will be shown in figures throughout.

3. Overview Over the LES and IFS Results

In the following, we will first give an overview of the atmospheric state, the cloud structure, and momentum profiles simulated in the LES and IFS to then dive into the underlying parametrizations and their uncertainties. The profiles of potential temperature and specific humidity for the two cases are shown in Figure 1. The vertical structure of the atmospheric state looks comparable for the case between the LES and the IFS. The two different times in the LES (10 and 60 h) show small differences, with a drier subcloud layer and a more moist profile at 800 hPa at 60 h. For CONSTRAIN, the IFS simulates a shallower mixed layer and a smoother inversion in comparison to the LES data.

3.1. Clouds

Figure 2a shows the domain-mean liquid water content at 10 h (unorganized cloud field) and 60 h (organized cloud field) in the LES. Between hour 10 and hour 60, the liquid water content increases and shows a top-heavy profile where the liquid water content increases with height in the LES. As clouds start to organize, the variability in the domain increases, as visible in the widening of the red and black shading. At 60 h, some subdomains contain hardly any clouds, while in other subdomains thick clouds appear, that show strong cloud top detrainment. Cloud fraction in the LES (Figure 2c) decreases as clouds organize. The IFS shows a deeper cloud layer and more liquid water content (Figure 2b). The maximum liquid water is simulated in the middle of the cloud layer. Convection is triggered in each ensemble member. While cloud fraction at cloud base is comparable between the LES and IFS, it decreases more quickly with height in the LES. However, the exact value of the cloud fraction in the LES depends on its definition. The cloud fraction in the LES is defined as the fraction of points whose cloud liquid water content exceeds $10^{-5} \text{ kg kg}^{-1}$, while in the IFS it is given by the cloud scheme and indicates the fraction of each grid box covered by clouds.

In the CONSTRAIN case, mixed-phase clouds develop at the top of the mixed layer (Figures 2e–2h). As the air is advected southward over warmer SST, the mixed layer deepens and the clouds shift upward (not shown). The focus will be on 31 January 2010, 03 UTC, when a well-mixed layer has developed and the

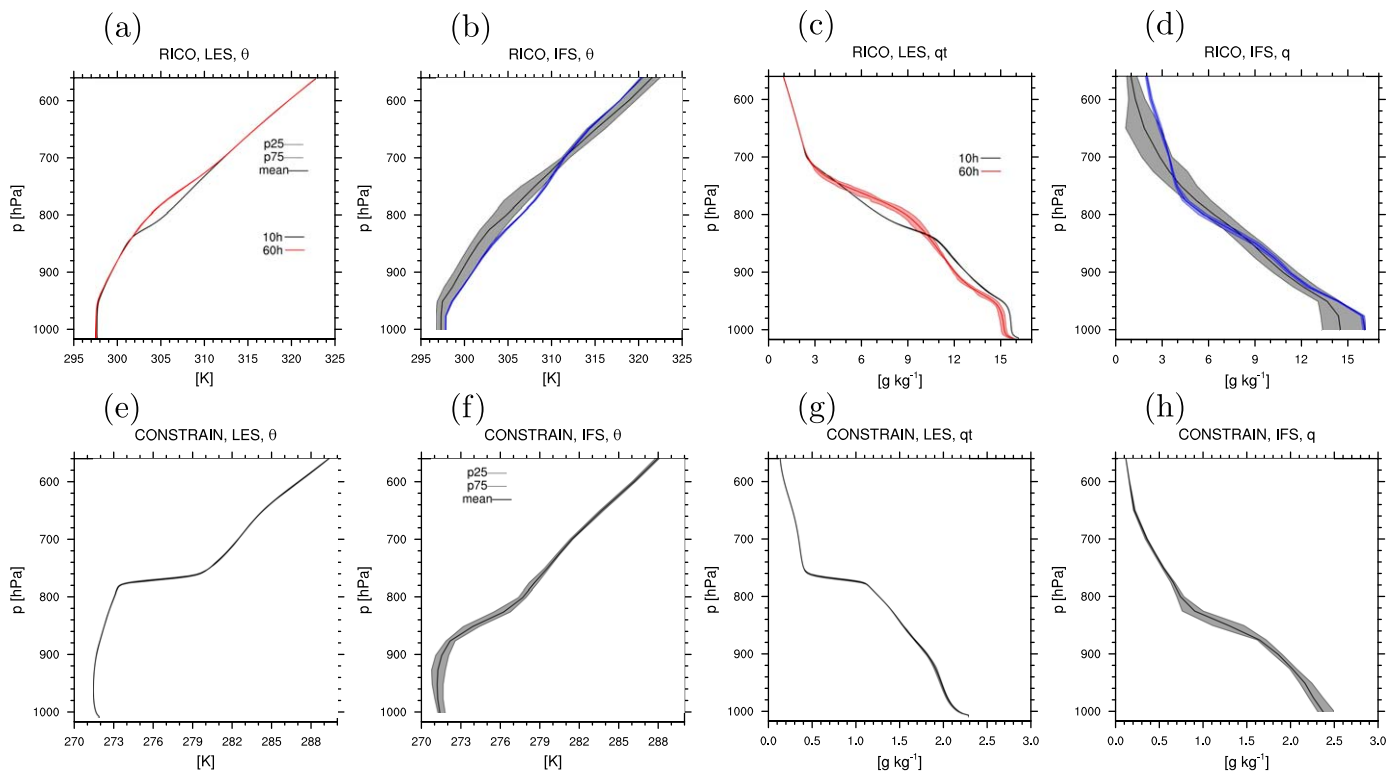


Figure 1. Vertical profiles of (a, b, e, and f) θ (K), (c, d, g, and h) specific humidity (g kg^{-1}) in the LES (Figures 1a, 1c, 1e, and 1g) and the IFS (Figures 1b, 1d, 1f, and 1h) for the RICO case at 10 and 60 h into the simulation for the LES and the average over the ensemble as defined in the text for (top row) the IFS and (bottom row) the CONSTRAIN case at 0300 UTC on 31 January 2010. At each level, the 25th percentile, mean and 75th percentile over all subdomains or ensemble members, respectively are selected. For RICO, the spread between ensemble members for 17 December 2004 is added by the blue bar in Figures 1b and 1d.

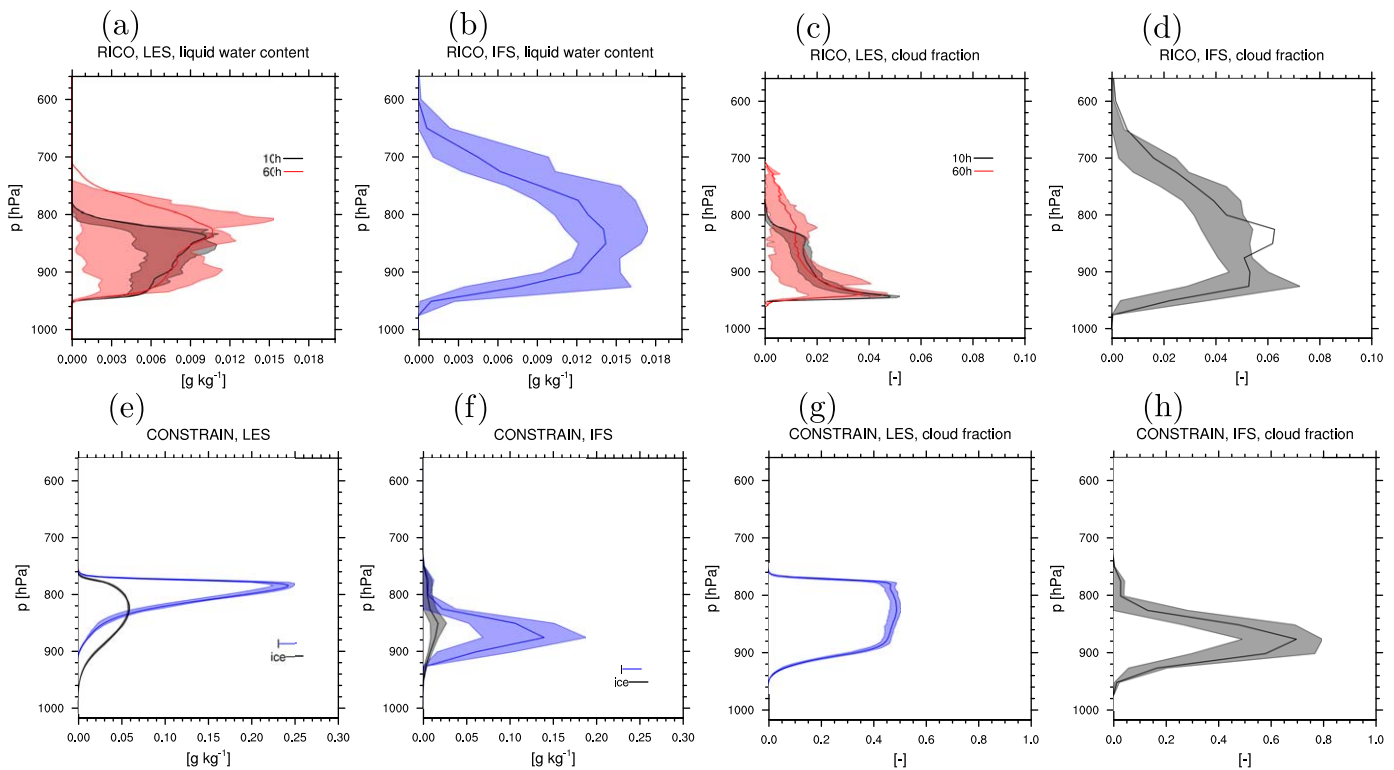


Figure 2. Liquid water content (g kg^{-1}) in (a, e) the LES data, (b, f) the IFS data and cloud fraction in (c, g) the LES data, (d, h) the IFS. (top row) The RICO case at 10 and 60 h into the simulation for the LES and the average over the ensemble as defined in the text for the IFS; (bottom row) the CONSTRAIN case at 0300 UTC on 31 January 2010. At each level, the 25th percentile, mean and 75th percentile over all subdomains or ensemble members, respectively are selected. For the CONSTRAIN case, the ice water content (g kg^{-1}) is added.

cloud layer is still well defined both in the LES and IFS simulations. This time of analysis is 4.5 h into the LES and 18 h into the IFS run. Since mixed-phase clouds are analyzed, the computation of the cloud fraction is adapted: grid points with a cloud liquid water content or ice water content larger than $10^{-5} \text{ kg kg}^{-1}$ are considered cloudy. Both liquid water and ice water content are larger in the LES than in the IFS simulation and the mixed layer is deeper. Moreover, the clouds dissolve earlier in the IFS. However, the IFS produces a larger cloud fraction.

3.2. Momentum

The zonal wind exhibits strong shear in the RICO case, decreasing from values from -8 m s^{-1} at cloud base to 0 m s^{-1} at the LES model top (Figure 3a). In the subcloud layer, the zonal wind decreases from -8 m s^{-1} at cloud base toward -6 m s^{-1} at the surface. The meridional wind is more or less constant with height, with a slight increase in the subcloud layer and decreasing values in the surface layer. The variability between the subdomains is relatively small and increases between 10 and 60 h of the simulation, especially in the boundary layer. The shape of the profile remains constant over time, with an increase of the wind shear toward later times of the simulation. Thus, the shape of the momentum profile is affected little by the cloud organization. The IFS places the low-level jet at lower elevations but shows an overall consistent picture with the LES for the zonal wind (Figure 3b). The relaxed meridional wind in the IFS shows a reasonable agreement with the LES albeit it exhibits smaller wind speeds in the boundary layer and larger shear in the free troposphere. A similar flow structure with a low-level jet in the zonal wind and a more or less constant profile in the meridional wind is found in ERA-Interim (not shown).

In the CONSTRAIN case, the meridional wind shows a strong increase with height (Figure 3c), that corresponds to the pronounced southerly flow during cold-air outbreaks. In particular, there is a distinct jump of the wind speed across the inversion. This jump is visible both in the LES and IFS, whereas it is more pronounced for the zonal wind in the LES than in the IFS. In accordance with the deeper mixed layer, this jump is situated 60 hPa higher in the LES.

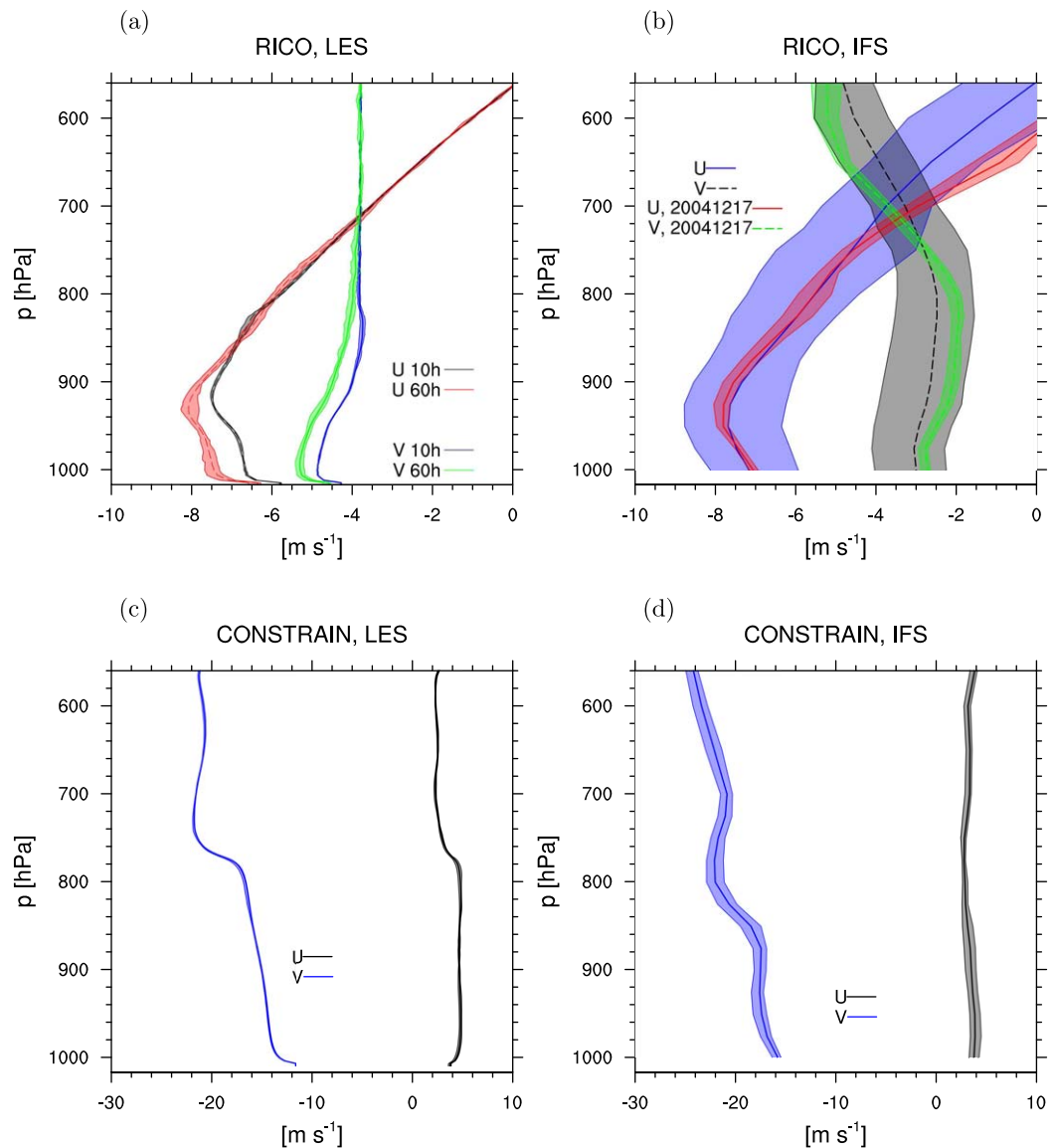


Figure 3. Zonal and meridional wind ($m s^{-1}$) in (a, c) the LES and (b, d) the IFS. (top row) The RICO case at 10 and 60 h into the simulation for the LES and the average over the ensemble as defined in the text for the IFS; (bottom row) the CONSTRAIN data at 0300 UTC on 31 January 2010. At each level, the 25th percentile, mean and 75th percentile over all subdomains or ensemble members, respectively are selected. For RICO, the spread between ensemble members for 17 December 2004 is added by the red and green bars in Figure 3b.

The presence of convective clouds within considerable wind shear is an indicator of CMT in both cases. Before diving into the detailed CMT analysis, we will first analyze the accuracy of the mass-flux approximation, and second the representation of the terms within the mass-flux approximation. For the RICO case, we will limit the analysis to the zonal wind at 60 h, as there are organized clouds within a low-level jet. In the CONSTRAIN case, we limit the analysis to the dominant meridional wind component.

4. Assumptions Underlying the Mass-Flux Approximation

The mass-flux framework is widely used to parametrize shallow convection. In this section, we will explore to what degree the mass-flux framework adequately approximates the total momentum transport. Both the validity of the mass-flux approximation for CMT and an adequate representation of the terms within the mass-flux approximation ultimately determine the accuracy of the momentum-flux representation. The large high-resolution LES data set offers the possibility to evaluate the variables involved within a typical CMT parametrization in detail. The following analysis relies entirely on LES output, thus the conclusions

from this section are independent of discrepancies between LES and IFS forcings. More details about the specific mass-flux formalism within the IFS are given in section A1.

4.1. Organized Momentum Flux Term Versus Total Momentum Flux

In the IFS, a bulk mass-flux approach is used to parametrize shallow convection [Tiedtke, 1989]. The mass-flux approach as first pioneered by Arakawa and Schubert [1974] decomposes the vertical flux (of momentum, heat, and moisture), $\overline{w'\chi'}$ of a variable χ into multiple terms:

$$\overline{w'\chi'} = \underbrace{\sigma_u \overline{w''\chi''}_u}_{\text{updraft}} + \underbrace{\sigma_d \overline{w''\chi''}_d}_{\text{downdraft}} + \underbrace{(1-\sigma_u-\sigma_d) \overline{w''\chi''}_e}_{\text{environment}} + \underbrace{\sigma_u(\overline{w}_u - \overline{w})(\overline{\chi}_u - \overline{\chi}) + \sigma_d(\overline{w}_d - \overline{w})(\overline{\chi}_d - \overline{\chi}) + (1-\sigma_u-\sigma_d)(\overline{w}_e - \overline{w})(\overline{\chi}_e - \overline{\chi})}_{\text{organized}}, \quad (1)$$

where χ can be u , v , and t or q , σ_u and σ_d are the updraft and downdraft fraction, respectively, and w is vertical velocity. Primed variables indicate deviations with respect to the domain-mean values, whereas double primes denote deviations to the updraft, downdraft, and environment, respectively. The first three terms on the RHS represent the flux associated with fluctuations of w and χ in the updraft, in the downdraft, and in the environment, respectively. The fourth term on the RHS represents the organized mass-flux term. Only this last term is considered in the mass-flux approximation, whereas the other terms are neglected:

$$\overline{w'\chi'}_{MF} \approx \sigma_u(\overline{w}_u - \overline{w})(\overline{\chi}_u - \overline{\chi}) + \sigma_d(\overline{w}_d - \overline{w})(\overline{\chi}_d - \overline{\chi}) + (1-\sigma_u-\sigma_d)(\overline{w}_e - \overline{w})(\overline{\chi}_e - \overline{\chi}). \quad (2)$$

$M_u = \rho \cdot \sigma_u \overline{w}_u$ denotes the upward convective mass flux, $M_d = \rho \cdot \sigma_d \overline{w}_d$ the downward convective mass flux, and $M_e = \rho \cdot (1-\sigma_u-\sigma_d) \overline{w}_e$ the mass flux in the environment. In the case of $\overline{w} \sim 0$, (2) reduces to

$$\overline{w'\chi'}_{MF} \approx M_u(\overline{\chi}_u - \overline{\chi}) + M_d(\overline{\chi}_d - \overline{\chi}) + M_e(\overline{\chi}_e - \overline{\chi}) \approx M_u(\overline{\chi}_u - \overline{\chi}) + M_d(\overline{\chi}_d - \overline{\chi}), \quad (3)$$

where under the so-called “small area approximation” the momentum flux in the environment has been neglected.

The mass flux is parametrized by an entraining plume, where entrainment dilutes the plume and detrainment represents the mass transfer into the environment:

$$\varepsilon - \delta = \frac{1}{M_u} \frac{\partial M_u}{\partial z} \quad \text{or} \quad \frac{\partial M_u}{\partial z} = E - D \quad (4)$$

with the fractional entrainment ε and detrainment δ , or the mass entrainment E and detrainment D , respectively.

The LES output is used to compute the various terms entering the computation of the momentum fluxes with the mass-flux approach in the IFS ((3) and (4)). The identification of updrafts and downdrafts in the LES data is done as follows: in the cloud layer, updrafts are those grid points where $w \geq 0.5 \text{ m s}^{-1}$, and the cloud liquid water content exceeds $10^{-5} \text{ kg kg}^{-1}$. Downdrafts are grid points where $w \leq 0.5 \text{ m s}^{-1}$. In the subcloud layer, two different approaches are pursued to identify updrafts and downdrafts. Applying the definition above for cloudy updraft points ($w \geq 0.5 \text{ m s}^{-1}$, cloud water $> 10^{-5} \text{ kg kg}^{-1}$) at the cloud base level yields an updraft fraction at cloud base $\sigma_{u,cb}$. In the first approach, all columns directly below identified updrafts and downdrafts at cloud base height are determined to be updrafts and downdrafts, respectively. In the second approach, a height-dependent threshold for w is employed. This threshold is determined such that the $(1-\sigma_{u,cb})$ th percentile of the w distribution constitutes the updrafts. This means that all grid points where the value of w exceeds the $(1-\sigma_{u,cb})$ th percentile are defined to be updrafts. Likewise the $\sigma_{d,cb}$ low-end part of the distribution constitutes the downdrafts. All grid points that are identified neither as updraft nor as downdraft belong to the environment. The different terms of (1) are extracted from the LES by taking the average over the entire domain (\overline{w} and $\overline{\chi}$), computing the mean values over updraft, downdraft, and environment areas (\overline{w}_u , \overline{w}_d , \overline{w}_e , $\overline{\chi}_u$, $\overline{\chi}_d$ and $\overline{\chi}_e$) and computing the deviation of w and χ with respect to this mean updraft, downdraft, and environment values ($w'' = w - \overline{w}_u$, $\chi'' = \chi - \overline{\chi}_u$, ...).

The different terms of (1) are illustrated in Figure 4 for $\chi = u$ for RICO and for $\chi = v$ for CONSTRAIN computed from the LES data. The total LES momentum flux consists of a resolved flux (black line) and a subgrid scale flux (dashed green line). Due to the fine grid spacing in the RICO LES runs ($\Delta x = 25 \text{ m}$), almost the entire

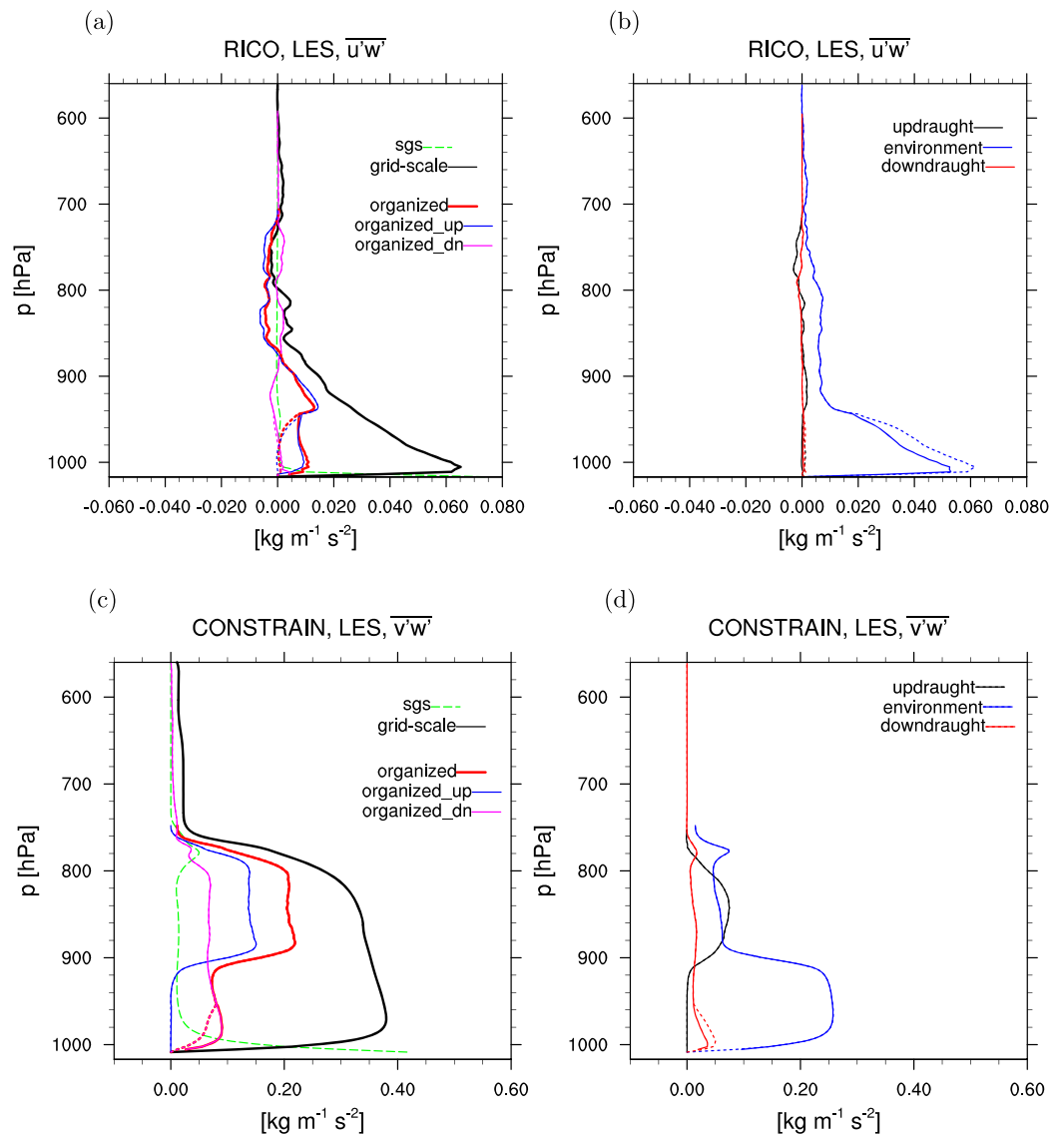


Figure 4. (a, c) Resolved (black) and subgrid scale (green dashed line) vertical flux of momentum ($\text{kg m}^{-1} \text{s}^{-2}$) in the LES. The total organized vertical flux of momentum ($\text{kg m}^{-1} \text{s}^{-2}$, cf., (1)) as recomputed from the LES data (red) is further split up into the updraught (blue) and downdraft (magenta) contribution. (b, d) The subplume fluxes in the updraught (black), environment (blue), and downdraft (red) components (cf., (1)) of the vertical flux as recomputed from the LES. (top row) The RICO case at 60 h and (bottom row) the CONSTRAIN case at 31 January 2010, 03 UTC. In the subcloud layer, the solid line corresponds to sampling those subcloud layer thermals that exceed the height-dependent w threshold, while the short-dashed line corresponds to sampling the areas below updrafts and downdrafts at cloud base.

flux is resolved by the LES and the subgrid scale component is small, except in the surface layer. Only the resolved variables from the LES are available for all further computations performed in our analysis. Thus, the contributions to the small subgrid scale fluxes (green dashed line in Figure 4) cannot be quantified and will thus be neglected. Generally, the upward flux of momentum is considerably stronger than the downward flux. Ideally, the organized mass-flux term (red line) should correspond to the total resolved flux (black line). Our results confirm the finding of Zhu [2015], that the mass-flux approximation does not capture the entire momentum flux. Indeed, Figure 4 shows that the organized mass-flux term covers only a part of the resolved vertical flux $\overline{\rho u'w'}$ and $\overline{\rho v'w'}$. A significant portion of $\overline{\rho u'w'}$ and $\overline{\rho v'w'}$ is carried by fluctuations in the environment (blue line in Figures 4b and 4d, third term on the RHS of (1)), which are neglected by the mass-flux approximation. This is becoming even more evident in the subcloud layer, where a large part of the flux is due to fluctuations in the environment. The two different approaches to isolate updrafts and downdrafts in the subcloud layer in the LES data yield different results for all the quantities considered, but

both approaches miss a large part of the flux. The fluctuations within the clouds and the downdrafts (black and red line in Figures 4b and 4d) are very small, thus it is justified to neglect them in the parametrization. One approach to deal with the missing momentum flux in the mass-flux approximation discussed in *Brown* [1999] is to scale the resulting fluxes by a constant factor to compensate for the neglected parts. The analysis here suggests that, if applied, this constant should be height dependent.

4.2. Pressure Gradient

Within the mass-flux approximation, the in-cloud values of \bar{u}_u and \bar{v}_u are required. These in-cloud values are challenging to parametrize, as the horizontal pressure gradient across updrafts accelerates the in-cloud winds [see e.g., *Kershaw and Gregory*, 1997]. The importance of the pressure-gradient term has been investigated for deep convection [e.g., *Grubišić and Moncrieff*, 2000], but little is known about its importance for shallow convection. The contribution of the pressure-gradient term is therefore often neglected in shallow convection parametrizations. We use the LES output to assess the magnitude of this pressure-gradient term and to evaluate how well this term can be reproduced by using different parametrizations that have been proposed in the literature.

Averaging the horizontal momentum equation and assuming steady state conditions gives

$$\frac{\partial}{\partial z}(\rho\sigma_u\overline{uW}_u) = E\bar{u} - D\bar{u}_u - \sigma_u \overline{\left(\frac{\partial p}{\partial x}\right)}_u \quad \text{and} \quad \frac{\partial}{\partial z}(\rho\sigma_u\overline{vW}_u) = E\bar{v} - D\bar{v}_u - \sigma_u \overline{\left(\frac{\partial p}{\partial y}\right)}_u, \quad (5)$$

where E and D denote the mass fluxes across the cloud boundaries. Applying the mass-flux formalism also to the in-cloud flux and using (4) results in

$$M_u \frac{\partial \bar{u}_u}{\partial z} = E(\bar{u} - \bar{u}_u) - \sigma_u \overline{\left(\frac{\partial p}{\partial x}\right)}_u \quad \text{and} \quad M_u \frac{\partial \bar{v}_u}{\partial z} = E(\bar{v} - \bar{v}_u) - \sigma_u \overline{\left(\frac{\partial p}{\partial y}\right)}_u. \quad (6)$$

Hence, the divergence of the vertical momentum flux is balanced by entrainment and detrainment across the updraft, plus the action of the pressure-gradient force. Within the mass-flux approximation, it means that the shear of in-cloud momentum is determined by entrainment across the updraft and the impact of the pressure gradient. The role of the pressure gradient in this balance is quantified by investigating the residual between the divergence of the momentum flux and the first term on the right-hand side of (6):

$$\mathcal{R} = M_u \frac{\partial \bar{u}_u}{\partial z} - E(\bar{u} - \bar{u}_u) \quad \text{and} \quad \mathcal{R} = M_u \frac{\partial \bar{v}_u}{\partial z} - E(\bar{v} - \bar{v}_u). \quad (7)$$

If the mass-flux approximation correctly represented the transport, \mathcal{R} should equal the pressure-gradient term. Thus, the difference between \mathcal{R} and the pressure-gradient term gives an indication about the errors introduced by applying the mass-flux formalism (horizontal averaging, steady state conditions, etc.). The pressure-gradient term is extracted from the LES by first calculating the local pressure gradient $\frac{\partial p}{\partial x}$ and $\frac{\partial p}{\partial y}$, respectively, by a forward difference. Then, these values are averaged over each updraft area as described above. As the local derivatives $\frac{\partial p}{\partial x}$ and $\frac{\partial p}{\partial y}$ cancel out in the interior of the updraft, the resulting values reflect the average pressure gradient across all updrafts.

Fractional entrainment ε and detrainment δ rates are extracted from the LES data following the bulk approach [see e.g., *de Rooy et al.*, 2012] using:

$$\frac{\partial \chi}{\partial z} = -\varepsilon(\bar{\chi}_u - \bar{\chi}_e), \quad (8)$$

$$\varepsilon - \delta = \frac{1}{M_u} \frac{\partial M_u}{\partial z}. \quad (9)$$

The total water mixing ratio (q_w in the CONSTRRAIN case, the ice mixing ratio is added) is employed as moist-conserved variable for χ . $\bar{\chi}_u$ are in-cloud values, whereas $\bar{\chi}_e$ are the values in the environment. Fractional entrainment/detrainment values from the LES are converted into values for mass entrainment E by $E = M_u \cdot \varepsilon$ and into mass detrainment D by $D = M_u \cdot \delta$ using the LES values for M_u . E and D will be analyzed in detail in section 5.

Figures 5a and 5b illustrate the individual terms of (6) and the residual (7). For RICO, the picture is much cleaner than for CONSTRRAIN. $\sigma_u \overline{\left(\frac{\partial p}{\partial x}\right)}_u$ is negative in the cloud layer and acts to decrease \bar{u}_u with height. Once the

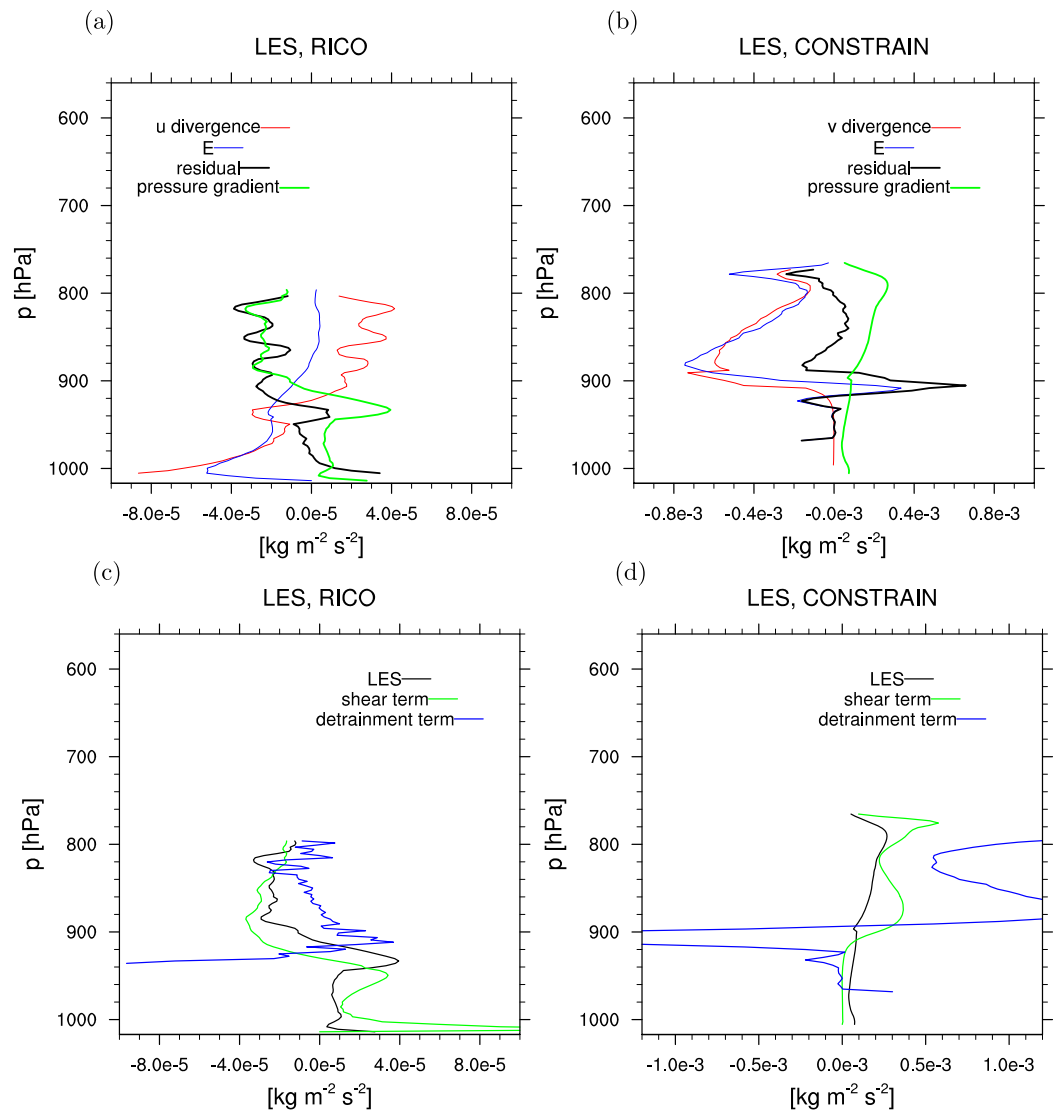


Figure 5. (top row) Momentum divergence (red) and entrainment term (blue) using (6), \mathcal{R} (black) and pressure-gradient term (green) for (a) u in RICO at 60 h and (b) v in CONSTRAIN at 31 January 2010, 03 UTC. (bottom row) Different approaches for parametrizing the pressure-gradient term (black) using vertical wind shear (green) or a modified detrainment rate (blue). (c) Displays u in RICO at 60 h and (d) v in CONSTRAIN at 31 January 2010, 03 UTC. The red lines in Figures 5a and 5b have been smoothed by applying a six-point running average to the data.

mass-flux approximation is applied to the in-cloud values (cf., (6)), the pressure-gradient term (green line) approximately matches the residual \mathcal{R} (black dashed line) in RICO. However, the magnitude of the pressure-gradient term is considerable, exceeding the entrainment term especially in the upper part of the cloud. Thus, entrainment does not balance the divergence of the momentum. Hence, the pressure-gradient term can explain the missing in-cloud momentum not captured by entrainment/detrainment within the mass-flux framework. Yet as shown in section 4.1, the fluxes within the environment are neglected by applying the mass-flux approximation and thus additional errors are introduced.

In CONSTRAIN (Figure 5b), the pressure-gradient term is roughly 1 order of magnitude larger than in RICO. $\sigma_v \left(\frac{\partial p}{\partial y} \right)_u$ is positive and acts to increase v with height. Within the mass-flux approximation, the entrainment term nearly matches the divergence of v , and thus \mathcal{R} becomes smaller than the pressure-gradient term. This indicates that additional terms on top of the pressure-gradient term are needed to capture \mathcal{R} . These could for example include terms representing the fluctuations in the environment.

Different practices for parametrizing the pressure-gradient term have been suggested, making use of the two terms on the RHS of (7). While *Wu and Yanai* [1994], *Kershaw and Gregory* [1997], or *Gregory et al.* [1997] emphasize the role of the vertical advection of momentum and parametrize it based on wind shear as

$$\sigma_u \left(\frac{\partial p}{\partial x} \right)_u = -C_1 M_u \frac{\partial u}{\partial z}. \quad (10)$$

Tiedtke [1989] focuses on the horizontal advection of momentum and thus increases the detrainment rate:

$$\sigma_u \left(\frac{\partial p}{\partial x} \right)_u = -C_2 D_u (\bar{u} - \bar{u}_u) \quad (11)$$

[see also *Brown*, 1999; *Grubišić and Moncrieff*, 2000]. The effect of these two different approaches is illustrated in Figures 5c and 5d using the values $C_1=0.7$ and $C_2=2$, respectively. While the black line shows the LES data, the blue and green lines illustrate the two different parametrizations. In RICO, the shear term shows positive values around cloud base and negative values in the middle of the cloud layer, decreasing to zero toward the cloud top. Except a downward shift in the altitude as compared to the LES, this matches the shape of the LES-derived pressure gradient adequately. The detrainment term also shows positive values near cloud base but fails to reproduce the negative values in the middle of the cloud layer. Around cloud base, both approaches show limitations. The shear term is shifted downward in comparison to the pressure-gradient term, while the detrainment formulation is shifted upward. The upward shift in the detrainment formulation is explained by the fact that in-cloud values \bar{u}_u are taken into account, which have undergone vertical transport already. The shear formulation on the other hand uses the local vertical wind shear, neglecting the vertical transport of momentum within the updrafts.

In contrast, for CONSTRAIN, both approaches overestimate the pressure-gradient term, in particular the detrainment formulation (11) that also produces a rather noisy profile.

5. Analysis of Parametrized Fluxes and Momentum

In the following section, we attempt to compare transport terms from LES and IFS directly. As was shown in section 3, some aspects of the two cases differ noticeably between LES and IFS, and it is likely that some of this is the result of forcing differences. One approach to gain information regardless consists of recomputing parametrized quantities of the IFS offline by replacing individual IFS quantities with those from the LES. This approach yields a measure of uncertainty that relates to the difference in the modeled state between LES and IFS.

In the following, we investigate to what extent the momentum flux, mass flux, E , D , and the in-cloud values of momentum are captured by the IFS parametrization, and how model errors in these variables impact the convective momentum fluxes.

5.1. Momentum Fluxes

Momentum is transported upward and downward by different processes. While in the LES, most of the flux is resolved (Figure 6), the momentum flux given by the IFS (Figure 7) is split into the resolved and unresolved part, with the unresolved part stemming from convection and diffusion, whereas the resolved flux stems from large-scale advection. The contribution of CMT to the total flux is considerable: CMT (illustrated by the red shading in Figure 7) is of comparable magnitude to the resolved momentum flux (shown by the green shading in Figure 7). In the RICO case, the zonal momentum flux is mostly positive in the LES data, apart from the upper cloud layer in the organized state (Figure 6). Except for the surface layer, most of the momentum flux is resolved and the subgrid scale part of the momentum flux is very small in the LES. In the IFS, the unresolved flux shows positive values in the subcloud layer but partly negative values in the cloud layer. These negative values are attributable to the missing positive momentum flux within the environment, which is neglected by the mass-flux approximation (cf., section 4.1). Important to note is that the momentum flux is mostly downgradient in the RICO case at all investigated time steps.

As in the RICO case, momentum fluxes are downgradient in CONSTRAIN (Figure 6) with a positive flux of meridional momentum up to the inversion. In the LES data, a larger fraction of the total flux is subgrid scale than in the RICO LES data. This is due to the coarser grid spacing of $\Delta x = 250$ m employed. The vertical flux of meridional momentum is positive and about an order of magnitude larger than the flux of zonal

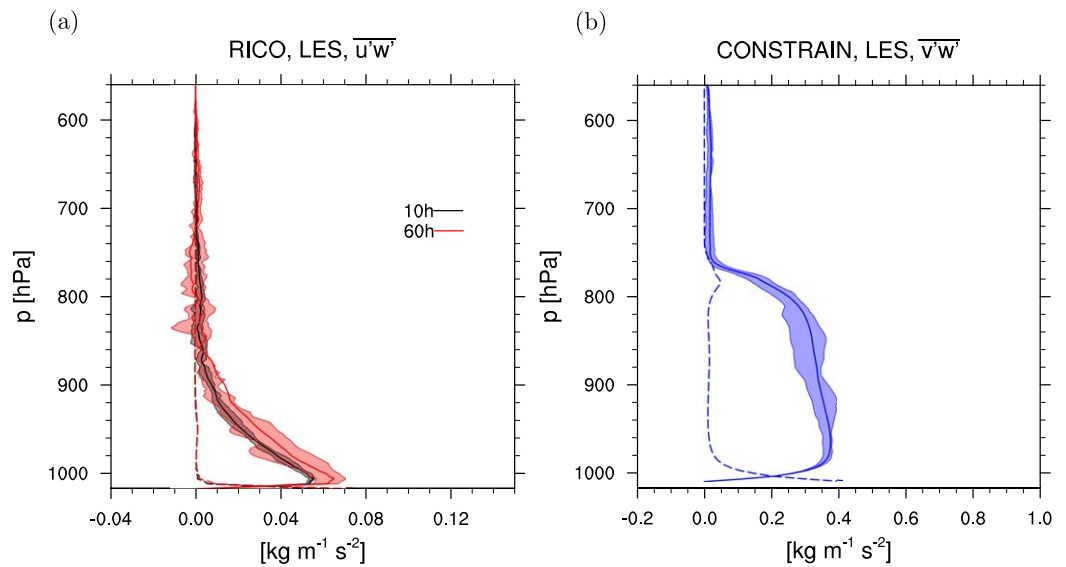


Figure 6. Momentum flux ($\text{kg m}^{-1} \text{s}^{-2}$) in the LES for (a) zonal momentum in RICO at 10 and 60 h into the simulation and (b) meridional momentum in CONSTRAIN at 0300 UTC on 31 January 2010. At each level, the 25th percentile, mean and 75th percentile over all subdomains are selected. The domain-mean subgrid scale component of the flux is added by the dashed line.

momentum in RICO. The IFS reproduces the strong positive flux of meridional momentum in the unresolved parts, again with very strong values near the surface. The underestimated boundary layer depth is reflected in a shallower flux layer. It should be noted that the resolved flux is considerably larger in the strongly baroclinic CONSTRAIN case.

The terms entering the convective part of the momentum fluxes are analyzed individually in the following. The aim is to understand the systematic errors inherent to the different approximations.

5.2. Mass Flux and Entrainment/Detrainment

Within the mass-flux approximation, an appropriate prediction of the convective mass flux and the in-cloud values is essential. Figure 8 illustrates M_u , E , and D as extracted from the LES. Moreover, we added the

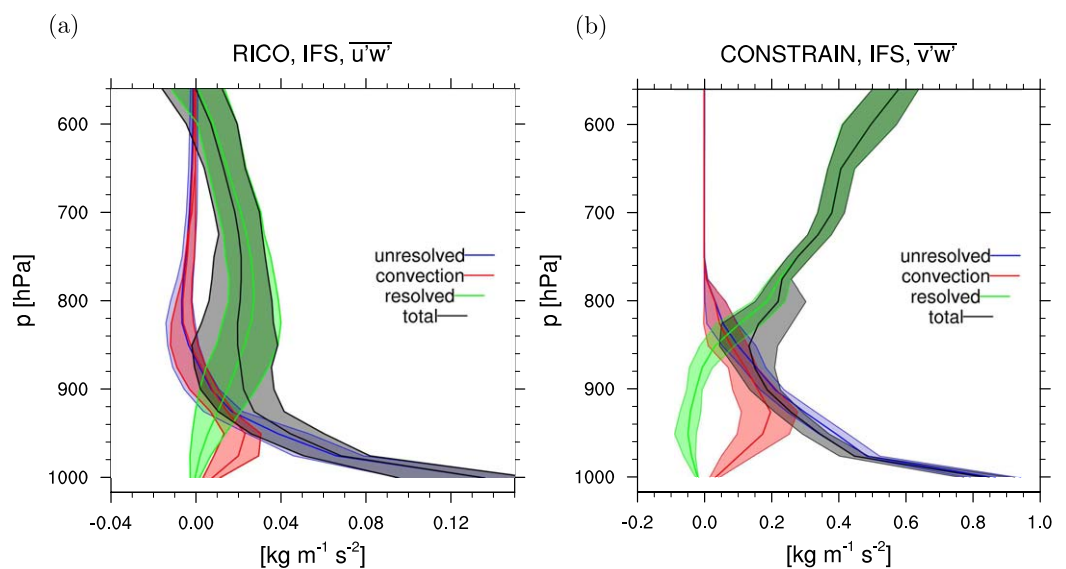


Figure 7. Momentum flux ($\text{kg m}^{-1} \text{s}^{-2}$) in the IFS for (a) the average $\overline{u'w'}$ over the ensemble as defined in the text for the IFS for RICO and (b) $\overline{v'w'}$ in CONSTRAIN at 0300 UTC on 31 January 2010. At each level, the 25th percentile, mean and 75th percentile over all ensemble members are selected.

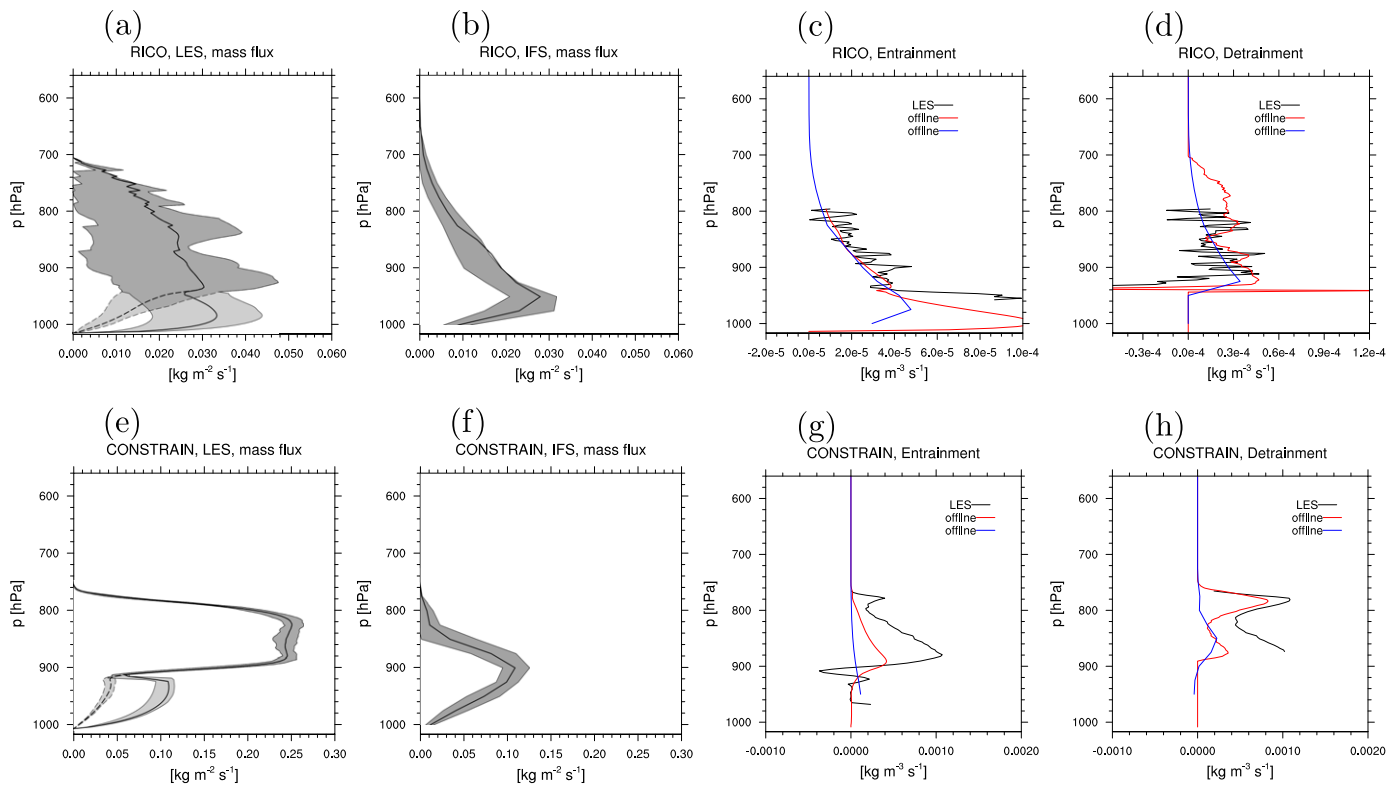


Figure 8. Upward convective mass flux ($\text{kg m}^{-2} \text{s}^{-1}$) from (a, e) the LES and (b, f) the IFS. In the subcloud layer, in the LES data, the solid line corresponds to sampling those subcloud layer thermals that exceed a certain threshold, while the dashed line corresponds to sampling the areas below individual cloud bases. (c, g) Rates of mass entrainment ($\text{kg m}^{-3} \text{s}^{-1}$) derived from the LES (black), obtained by performing an offline calculation using the IFS equations but the LES values (red solid line), and obtained by performing an offline calculation using the IFS equations and the IFS values (blue solid line). (d, h) Same as Figures 8c and 8g but for *D*. (top row) The RICO case at $t = 60$ h; (bottom row) the CONSTRAIN case at 31 January 2010, 03 UTC.

entrainment and detrainment from offline calculations employing the IFS formulation but using the LES or ensemble-mean IFS values for mass flux and environmental values as input (see *Bechtold et al.* [2014], and section A2 for details on the parametrizations). In the RICO case, the cloud base convective mass flux, which is determined by the closure is very well predicted by the IFS (Figures 8a and 8b). The IFS convective mass flux drops off slightly faster than the LES data but shows an overall good agreement.

In the CONSTRAIN case (Figures 8c and 8d), the convective mass flux is considerably larger in the LES than in the IFS simulation, and the cloud layer is significantly deeper. Moreover, it shows a quick decrease with height in the IFS, whereas the LES suggests a profile which is more or less constant with height throughout the cloud layer. As seen for the RICO case, an accurate prediction of the cloud base convective mass flux is crucial for a correct representation of the entire profile. The mass-flux profile is therefore underestimated because the value at the cloud base is underestimated.

Figures 8c, 8d, 8g, and 8h show the values for the LES-derived mass entrainment and detrainment using q_t as conserved tracer (black line, in the CONSTRAIN case the ice mixing ratio is added, cf., section 4.2). *E* and *D* are recalculated using the IFS parametrization routine but using the LES values for relative humidity and M_u (red line) or using the IFS values for relative humidity and M_u (blue line) (see section A2 for further details).

Offline-calculated values for entrainment rates using both LES and IFS variables as input fit very well the LES-derived values for RICO throughout the entire cloud layer. Detrainment rates show a maximum around cloud base, a distinct minimum in the middle of the cloud layer, and a second maximum around cloud top, representing the organized detrainment. This behavior is found in the LES data and the offline calculations with comparable magnitudes.

In CONSTRAIN, LES-derived entrainment and detrainment values are larger than offline-computed values for entrainment and detrainment. This is especially true if the relative humidity from the IFS is employed in

the computations (blue line in Figures 8g and 8h). As already visible for the RICO case, D shows a minimum in the middle part of the cloud and a peak at cloud top, representing the organized detrainment. Given the difference in the mass-flux profiles, only the E and D profiles computed with the IFS formulation but using as input the LES mass-flux and environmental profiles reasonably agree with the LES data.

5.3. In-Cloud Values

For the computation of the momentum flux, the momentum within the updraft \overline{u}_u and \overline{v}_u , respectively is required (cf., (3)). There are several challenges connected with their prediction. First, as emphasized earlier, the horizontal winds are affected by the horizontal pressure gradient across the updraft, which accelerates the in-cloud winds [see e.g., *Kershaw and Gregory, 1997*]. Second, values for the horizontal momentum at cloud base are unknown. In the IFS, the value at cloud base $u_{u,cb}$ is set to the environmental value at the departure level for convection. The in-cloud values for u are then predicted going upward from cloud base (cf., (5)):

$$\frac{\partial M_u \overline{u}_u}{\partial z} = E_u \overline{u} - D_u \overline{u}_u - \underbrace{\sigma_u \left(\frac{\partial p}{\partial x} \right)_u}_{\text{pressure-gradient term}} \quad (12)$$

Below cloud base, a linear decrease of the momentum flux with height is assumed. The pressure-gradient term is currently neglected in the IFS in the prediction of \overline{u}_u and \overline{v}_u . Finally, a correction term is applied to the updraft velocities:

$$\overline{u}_u = \overline{u}_u - \min(|\overline{u}_u|, u_{pert}) \text{sign}(\overline{u}_u) \quad \text{and} \quad \overline{v}_u = \overline{v}_u - \min(|\overline{v}_u|, u_{pert}) \text{sign}(\overline{v}_u) \quad (13)$$

with $u_{pert} = 0.3 \text{ m s}^{-1}$. Hereby the updated formulation for the correction term as described in *Schlemmer et al. [2016]* is used that removes a discontinuity at \overline{u}_u and $\overline{v}_u = 0 \text{ m s}^{-1}$.

Figures 9a, 9b, 9d, and 9e show the difference $\overline{u} - \overline{u}_u$ or $\overline{v} - \overline{v}_u$, respectively. In RICO, in the LES data, the difference is positive in the lower part of the clouds, indicating that the value of the in-cloud momentum is smaller than the domain-mean value. In the RICO case, where the low-level jet prevails, in-cloud momentum becomes larger than the domain-mean value in the upper part of the clouds, resulting in a negative difference. The IFS reproduces this behavior and shows positive values for $\overline{u} - \overline{u}_u$ and the shift toward negative values for RICO in the upper part of the cloud layer. Yet values are overestimated when considering the ensemble mean. Within the subcloud layer, IFS values are too large and the IFS data are outside the range of the LES, whereas it captures the LES values in the cloud layer.

In CONSTRAIN, the LES suggests a profile of $\overline{v} - \overline{v}_u$ that is more or less constant with height and shows small variability between the subdomains. There is a distinct jump across the inversion. The IFS predicts a profile that decreases throughout the cloud layer but misses the jump across the inversion. The different shape of the profile can be explained by the different shape of the mass-flux profile that shows a quick decrease with height (see section 5.2).

In order to further test the validity of the employed parametrization, the values for \overline{u}_u and \overline{v}_u are step by step recalculated offline using LES values. These offline-derived values are then in turn compared to LES values for in-cloud momentum. To this end, (12) is integrated inserting directly LES-derived data for $u_{u,cb}$, \overline{u} , M_u , E_u , and D_u . The red lines in Figure 9 display these recalculated values with (dashed red line) and without (solid red line) the correction term (13). Ideally, the red dashed lines should match the black lines in Figures 9c and 9f. The first apparent issue is the mismatch of the cloud base value for \overline{u}_u (in RICO) and \overline{v}_u (in CONSTRAIN). Using the momentum at the departure level for convection as a proxy for the cloud base values leads to an underestimation of both $u_{u,cb}$ and $v_{u,cb}$. The correction term thus deteriorates \overline{u}_u and \overline{v}_u . In RICO, the opposite picture emerges for v : the parametrization overestimates \overline{v}_u and thus the correction term improves the values of \overline{v}_u (not shown). The influence of the pressure-gradient term onto \overline{u}_u and \overline{v}_u is illustrated by the green dashed line, for which the LES-derived pressure-gradient term has been added for the in-cloud momentum (cf., (12)). While the effect of the pressure gradient is small near cloud base, it increases toward the cloud top. It pulls the in-cloud values toward the mean LES profile in RICO, yielding a better matching profile with height. In CONSTRAIN, the offline-calculated values for \overline{v}_u are smaller than the LES values and exhibit too much wind shear. Inclusion of the pressure-gradient term even increases the shear, deteriorating the profile of \overline{v}_u . A general finding from the analysis is that retrieving cloud base values for both convective mass-flux and in-cloud momentum is crucial, but difficult. The shape of the vertical profiles

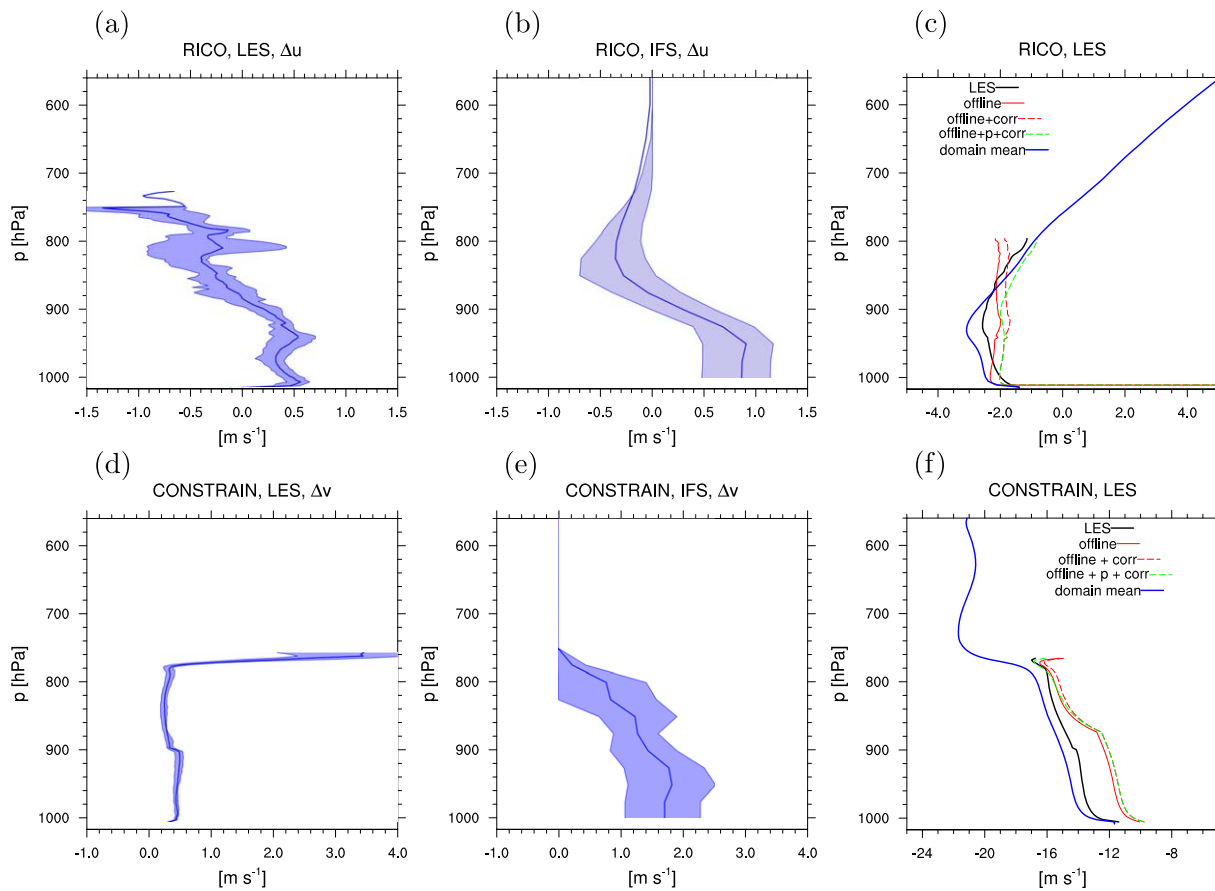


Figure 9. Difference between in-cloud momentum and domain-mean momentum $\Delta u = \bar{u} - \bar{u}_u$ or $\Delta v = \bar{v} - \bar{v}_u$, respectively for (a, d) the LES data and (b, e) the IFS. (c, f) The in-cloud momentum as extracted from the LES (black solid), recalculated using LES values following the IFS routines (red), recalculated using LES values following the IFS routines and adding the pressure-gradient term (green dashed) and domain-mean values from the LES (blue). The effect of applying the perturbation to the in-cloud values is illustrated by the dashed red line. (top row) Displays values for u for RICO valid at 60 h for the LES and the ensemble average for the IFS; (bottom row) shows v for CONSTRAIN valid at 31 January 2010, 03 UTC.

on the other hand is given by entrainment, detrainment, and the convective mass flux, which are very well captured in RICO but show deficiencies in CONSTRAIN.

5.4. Reconstructing Momentum Fluxes

Finally, the terms M_u , \bar{u}_u , \bar{u} , \bar{v}_u , and \bar{v} are taken together to retrieve the updraft convective momentum fluxes $\rho \overline{u'w'_u} \approx M_u(u_u - \bar{u})$ and $\rho \overline{v'w'_u} \approx M_u(v_u - \bar{v})$ (cf., (3)). To get an estimate of the error introduced within each variable, we plot different combinations of LES-derived and IFS-derived values for M_u and \bar{u}_u and compare them to the organized momentum flux as extracted from the LES. These estimates are shown together with the LES and IFS data in Figure 10. The analysis is only done for RICO, as in CONSTRAIN the IFS simulates a different boundary layer height, which makes the analysis hard to interpret. Figure 10 suggests that for the RICO case an appropriate representation of the in-cloud values of momentum is more critical than the representation of convective mass flux. Using the mass flux from the IFS (which was shown to be well represented) but the in-cloud values from the LES (blue line) yields a better result than using the in-cloud values from the IFS in combination with the convective mass flux from the LES (red line). However, the convective mass flux and the entrainment/detrainment rates also enter the prediction of the vertical profiles of in-cloud values (cf., (12)). Thus, it is difficult to separate these two players entirely.

6. Ensemble Spread and Uncertainty

Subsampling the LES as described in section 2.3 provides a measure of spatial variability. The SPP perturbations applied to the convection parameterization generate an ensemble of forecasts that represents the multitude of convection profiles that the large-scale environment can produce for the parameter

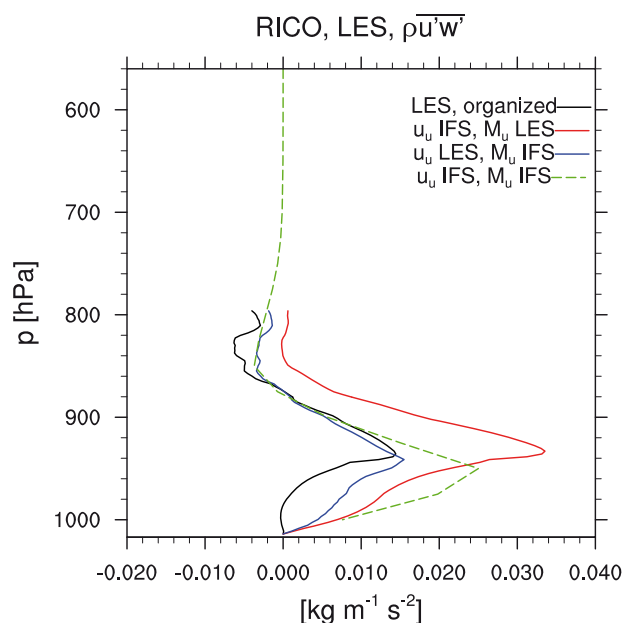


Figure 10. Upward organized convective momentum flux ($\text{kg m}^{-1} \text{s}^{-2}$) as extracted from the LES (black), recalculated using IFS values for $\overline{u'u}$ but M_u from the LES using (3) (red), recalculated using LES values for $\overline{u'u}$ but M_u from the IFS using (3) (blue), and values from the IFS (green) valid at 60 h in RICO.

uncertainty inherent in the convection scheme. While both produce spread, this spread is not entirely comparable. In particular, neither one is a good measure of uncertainty due to the (disparate) forcings. An additional IFS ensemble with perturbations of the initial conditions might provide a more appropriate measure of uncertainty related to the forcing. Also, as individual simulation days in the IFS are treated as separate ensemble members, the spread contains also a measure of day-to-day variability. Day-to-day variability explains much of the spread in the RICO winds (comparing the red bar to the blue bar, and the green bar to the black bar in Figure 3a), for example. Nevertheless, comparing the LES and SPP spread here still provides information insofar as a disagreement between simulations (i.e., nonoverlapping spread) indicates that the IFS cannot reproduce the LES results, given the forcing and known uncertainties of the convection parameters.

The SPP generates a large spread for all quantities considered above. For the tropical convective clouds with strong organization of the cloud field, the subsampling of the LES data suggest that this large spread is justified. In the extratropical, more stratiform case, the LES shows little organization and a comparatively homogeneous cloud field, whereas the SPP invariably gives a large spread. Stratiform layers of clouds are known to show a more homogeneous structure than convective clouds [e.g., Cotton *et al.*, 2011], which is reflected in the identified reduction of spread within the LES. On the other hand, the LES results can also be very sensitive to the details within the microphysics scheme (S. de Roode, 2017, personal communication), especially as mixed-phase clouds are present (e.g., assumptions about the processes of sedimentation, accretion, and evaporation/melting). Thus, ideally one would like to perform an SPP-like approach for the LES as well, as it is unclear if the LES-spread is representative for the full uncertainty. The SPP within the IFS in contrast to the LES does not show a reduction in spread between the tropical and the extratropical case.

In RICO, the LES presents a large spread for the clouds, both in terms of liquid water content and cloud tops (cf., Figure 2). As a result of this, all quantities that are directly connected to the cloud dynamics, such as mass-flux, in-cloud values and CMT show a large spread in the LES subdomains. The SPP gives a comparable estimate for the spread in convection-related variables. The profiles of “environmental” variables, such as momentum, temperature, and humidity, show little variability between the subdomains in the LES (see Figure 1). The SPP in contrast tends to give an equally large spread to the environmental variables as to the convection-related quantities. This can to a large degree be explained by the day-to-day variability of the IFS run. This becomes apparent by comparing the blue bar in Figures 1b and 1d which displays the variability between ensemble members for one individual day, with the gray bar that includes the day-to-day variability. Although the simulation is run over the “undisturbed” RICO period, the profiles differ considerably from day to day. Certainly, the LES which is an idealized composite case misses this variability in the environmental variables, as there is only constant, prescribed large-scale forcing in the LES domain. Any uncertainty related to large-scale disturbances affecting the domain of interest is thus missing. This problem could be tackled by running additional LESs prescribing the forcing from the individual RICO days. Yet the simulations are very expensive, and the cloud field takes a long time to organize itself. A further cause for the discrepancy between LES and SPP spread could be that the SPP overestimates the feedback from the convective to the large-scale variables and as a result the variability of the “environmental” variables such as temperature, humidity, or momentum. The narrower spread in the LES could also indicate that the forcing in the LES is uncorrelated in time and the forcing differences average out in time.

For the more stratiform CONSTRAIN case, the LESs suggest a considerably smaller spread within the domain for all quantities (see e.g., Figure 2 for clouds or Figure 8 for mass flux). Yet for the IFS runs, the spread is not decreased between RICO and CONSTRAIN. As described above, the LES is probably overly confident, as the case is sensitive to the specific treatment of the microphysical processes.

Throughout the analysis, we have identified in-cloud values for momentum and cloud base convective mass flux as critical variables. The SPP alleviates some of these challenges, especially for the vertical profiles for in-cloud momentum (cf., Figure 9). The SPP provides some spread to the in-cloud momentum that yields an overlap between LES-derived variables and IFS-simulated ones. Nevertheless, the SPP is unable to counterbalance systematic errors that are for example found for $v_{u,cb}$ or convective mass flux in CONSTRAIN. For these, the set of IFS values lies outside the set of LES-derived values.

The SPP finally perturbs the momentum fluxes themselves in the presence of deep convection to mimic upgradient momentum transport. Judging from the analysis of the RICO and CONSTRAIN case, there is hardly any upgradient transport. It would however be interesting to investigate further regions, in which upgradient transport may occur, as e.g., within the MJO or along low-level jets related to frontal system. In order to capture those systems, one would need a less idealized setup than currently used for the high-resolution simulations and a considerably larger domain. The probability of occurrence for upgradient transport within the SPP could then be tuned accordingly.

7. Conclusions

We have investigated uncertainties related to the convective momentum transport and its representation in the IFS convection scheme for two different cases of shallow convection over ocean surfaces. For the first case, RICO, the LES data show considerable organization of the cloud field over the course of the simulation. Even though the spatial cloud pattern changes markedly with the organization, the characteristics of the momentum flux change little. Despite areas of upscale momentum transport in the organized state, the net effect of convection is to act as “cumulus friction” and to reduce the shear. The second case, CONSTRAIN, displays the deepening and breakup of stratocumulus clouds developing within strong wind shear in a cold-air outbreak. In both cases, the convective momentum flux is downgradient and the flux divergence considerable, amounting to net accelerations of $1 \text{ m s}^{-1} \text{ h}^{-1}$.

Using the mass-flux framework to parametrize the convective momentum fluxes, parts of the fluxes are missed. Especially in the subcloud layer, but also within the cloud layer, there are considerable fluxes in the environment that are omitted by the mass-flux approximation. A further shortcoming of the mass-flux approximation manifests itself in the in-cloud values of momentum. The evolution of the in-cloud momentum profile in the vertical is not captured by entrainment, detrainment, and the pressure-gradient term alone, but some unknown additional terms are missing, which could, e.g., be related to nonsteady conditions or in-cloud fluctuations.

We have dissected the terms entering the parametrization of the momentum flux by comparing the individual terms of the IFS shallow convection parametrization to the LES data. We have also integrated offline the IFS in-cloud momentum equations using LES data. A satisfactory representation of entrainment and detrainment yields an appropriate representation of the convective mass-flux profile. Yet the value of cloud base convective mass-flux gauges the magnitude of the entire mass-flux profile. While cloud base mass flux is well predicted for the subtropical RICO case, it tends to be underestimated in the extratropical case. In-cloud momentum is the most uncertain quantity, an improvement of its representation could be beneficial for the entire convective momentum transport. While the parametrizations yield a decent shape of the vertical profile, assigning the value for in-cloud momentum at cloud base is crucial, as it sets the magnitude of the entire profile. Cloud base values for in-cloud momentum proved to be underestimated in some cases, but overestimated in other instances. Thus, the correction term used at present in the IFS shallow convection scheme works successfully in some cases, while it worsens results in other cases. This uncertainty is absorbed in the IFS stochastically perturbed parametrizations (SPP) scheme by perturbing the entire resulting CMT profile.

Including the pressure gradient across updrafts into the prediction for in-cloud momentum improves the shape of the vertical profile of \overline{u} and \overline{v} , especially in the upper part of the cloud. Thus, it could be worthwhile to implement any of the discussed methods into the parametrization and evaluate them in a global

model context; so far, preliminary tests remained inconclusive about distinctive advantages. Yet the pressure-gradient term does not capture the entire residuum between the divergence of the momentum flux and the entraining plume model. Using the mass-flux approximation to deduce the momentum flux introduces errors of similar order of magnitude as neglecting the pressure-gradient term.

The SPP approach captures to some extent the uncertainty related to CMT. The comparison between the IFS ensemble and the LES ensemble is however challenging due to strong day-to-day variability within the IFS that is absent in the LES. For the RICO case, this variability accounts for a large part of the IFS spread. The larger spread in the IFS ensemble could also indicate that the temporal and spatial correlations of the perturbation coefficients within the IFS are too strong. The direct comparison between LES and IFS results is hindered by differences in the forcing and between the resultant cloudy model state. A more satisfactory comparison may hopefully be obtained in the future by applying the same methodologies to cases where LES and IFS forcing are more alike. Projects like for example the LES ARM Symbiotic Simulation and Observation (LASSO; <https://doi.org/10.5439/1256454>) framework promise to deliver a suite of more realistically forced and observationally constrained cases for use in model evaluation. Future work might also benefit from extending the ensemble methods to include both initial perturbations and SPP.

While the net momentum flux is directed downgradient in the current study, it would be interesting to further consider a case with counter-gradient momentum flux, in which CMT accelerates the mean flow. It is however uncertain, how often these flow situations occur and how much they feed back onto the larger scales. While there are patches of counter-gradient CMT in the investigated RICO case, the net effect remains downgradient. These cases would however be valuable to get an estimate on the amount of upgradient transport that the SPP should imitate by perturbing the momentum flux.

It would be instructive to extend the work on CMT to larger-scale high-resolution contexts that are moreover closer to reforecasts. These would first of all enable a cleaner comparison between the high-resolution and the parametrized runs. Second, capturing entire synoptic or MJO systems may yield conditions generating counter-gradient CMT.

Appendix A: Parametrizations Employed in the IFS

In the following, a short summary of the convection and diffusion parametrizations used in the IFS is given. More details can be found in ECMWF [2015].

A1. Convective Momentum Transport

The contribution from cumulus convection to the large-scale budget equations of momentum in pressure coordinates are

$$\left(\frac{\partial \bar{u}}{\partial t}\right)_{cu} = g \frac{\partial}{\partial p} [M_u(\bar{u}_u - \bar{u}) + M_d(\bar{u}_d - \bar{u})] \quad (A1)$$

and

$$\left(\frac{\partial \bar{v}}{\partial t}\right)_{cu} = g \frac{\partial}{\partial p} [M_u(\bar{v}_u - \bar{v}) + M_d(\bar{v}_d - \bar{v})] \quad (A2)$$

with the updraft convective mass flux M_u , the downdraft convective mass flux M_d , the acceleration of gravity g , pressure p , the updraft values for momentum \bar{u}_u and \bar{v}_u , and the downdraft values for momentum \bar{u}_d and \bar{v}_d . Below cloud base, a linear decrease of the momentum flux toward zero at the surface is prescribed. It is assumed that the cloud ensemble is in steady state. Thus, the equation for convective mass flux in the updraft can be written as

$$-g \frac{\partial M_u}{\partial p} = E_u - D_u \quad (A3)$$

with the entrainment rate E_u and the detrainment rate D_u into the updraft (these will be detailed in section A2). Updraft value for the momentum \bar{u}_u and \bar{v}_u become

$$-g \frac{\partial (M_u \bar{u}_u)}{\partial p} = E_u \bar{u} - D_u \bar{u}_u \quad (A4)$$

and

$$-g \frac{\partial(M_u \bar{v}_u)}{\partial p} = E_u \bar{v} - D_u \bar{v}_u. \quad (\text{A5})$$

The vertical integration of (A3), (A4), and (A5) requires knowledge of the cloud base convective mass flux $M_{u,cb}$ and the cloud base values of \bar{u}_u and \bar{v}_u , respectively. For shallow convection, a moist static energy equilibrium is assumed: $M_{u,cb}$ then follows from the ratio of the integrated moist static energy tendency (resulting from the dynamics, the radiation, and the turbulent diffusion) and the updraft moist static energy excess at cloud base.

As illustrated in section 5.3, the determination of \bar{u}_u and \bar{v}_u is not straightforward. The value at cloud base is set to the environmental value at the departure level for convection. Finally, the updraft velocities are decreased by a constant perturbation u_{pert} :

$$\bar{u}_u = \bar{u}_u - \min(|\bar{u}_u|, u_{pert}) \text{sign}(\bar{u}_u) \quad \text{and} \quad \bar{v}_u = \bar{v}_u - \min(|\bar{v}_u|, u_{pert}) \text{sign}(\bar{v}_u). \quad (\text{A6})$$

For the downdraft, an analog set of equations is used:

$$-g \frac{\partial M_d}{\partial p} = E_d - D_d \quad (\text{A7})$$

with the downdraft entrainment rate E_d and detrainment rate D_d . Downdraft value for the momentum \bar{u}_d and \bar{v}_d becomes

$$-g \frac{\partial(M_d \bar{u}_d)}{\partial p} = E_d \bar{u} - D_d \bar{u}_d \quad (\text{A8})$$

and

$$-g \frac{\partial(M_d \bar{v}_d)}{\partial p} = E_d \bar{v} - D_d \bar{v}_d. \quad (\text{A9})$$

Downdrafts are assumed to originate from the Level of Free Sinking (LFS). The convective mass flux at the LFS is set proportional to the cloud base updraft value:

$$M_{d,LFS} = -\eta M_{u,cb} \quad (\text{A10})$$

with $\eta = 0.3$.

The updraft value for the momentum at the LFS is set to the average between the environmental value at the LFS and the updraft:

$$u_{d,LFS} = 0.5 \cdot (\bar{u}_{LFS} - \bar{u}_{u,LFS}) \quad \text{and} \quad v_{d,LFS} = 0.5 \cdot (\bar{v}_{LFS} - \bar{u}_{u,LFS}). \quad (\text{A11})$$

A2. Entrainment and Detrainment

Entrainment and detrainment rates represent the horizontal mass exchange between the convective plumes and the environment. They thus crucially influence the vertical profile of convective mass flux, which in turn determines the vertical transport of the required quantities. In the IFS, updraft entrainment rates are parametrized as

$$E_u = \varepsilon_u f_\varepsilon \frac{M_u}{\bar{\rho}} (1.3 - RH) f_{scale}, \quad (\text{A12})$$

with the fractional entrainment $\varepsilon_u = 1.75 \times 10^{-3} \text{ m}^{-1}$, the density of the environment $\bar{\rho}$, and the relative humidity of the environment RH . The vertical scaling function f_{scale} is defined as

$$f_{scale} = \left(\frac{q_s(\bar{T})}{q_s(\bar{T}_{base})} \right)^3, \quad (\text{A13})$$

with the saturation specific humidity q_s and temperature T . f_ε is set to 1 for deep convection, and 2 for shallow and midlevel convection.

Turbulent detrainment rates for shallow convection within updrafts are assumed to occur (1) through turbulent exchange and (2) through organized outflow at the cloud top:

$$D_u = D_u^{(1)} + D_u^{(2)}. \quad (A14)$$

The turbulent component is set proportional to the entrainment rate:

$$D_u^{(1)} = E_u(1.6 - RH). \quad (A15)$$

Thus, the relative humidity of the environment influences both entrainment and detrainment. Drier environments increase both entrainment and detrainment leading to a faster dilution of convective plumes.

The calculation of the organized detrainment $D^{(2)}$ relies on the updraught kinetic energy K_u that is obtained from

$$\frac{\partial K_u}{\partial z} = -\frac{\mu_u}{M_u}(1 + \beta C_d)2K_u + \frac{1}{f(1+\gamma)}g\frac{T_{v,u} - \bar{T}_v}{\bar{T}_v} \quad (A16)$$

with the mixing coefficient μ_u which is equal to the entrainment rate ($E_u\bar{\rho}$), or the detrainment rate ($D_u^{(1)}\bar{\rho}$) if the former is zero. β is set to 1.875, $C_d=0.506$ is a drag coefficient, $T_{v,u}$ is the virtual temperature of the updraught, and \bar{T}_v the virtual temperature of the environment, $\gamma=0.5$ is a virtual mass coefficient, while the factor $f=2$. The cloud base value for K_u is set by choosing the updraught vertical velocity w_u at cloud base as $w_{u,cb} = 1 \text{ m s}^{-1}$ and setting $K_{u,cb} = \frac{w_{u,cb}^2}{2}$.

The organized detrainment is finally retrieved as

$$D_u^{(2)} = \frac{M_u}{\bar{\rho}\Delta z} \left[1 - (1.6 - RH) \sqrt{\frac{K_u(z + \Delta z)}{K_u(z)}} \right]. \quad (A17)$$

A3. Eddy-Diffusivity Mass-Flux Approach

An Eddy-Diffusivity Mass-Flux (EDMF) approach is used to compute the exchange coefficients within the well-mixed part of convective boundary layers [Köhler *et al.*, 2011]. In the case of shallow convection, the EDMF approach is applied only between the surface and cloud base. Moreover, the mass-flux part of the EDMF is turned off, as it is assumed that the nonlocal transport by the convection scheme will take care of this mass-flux part. Thus, only local diffusion is done by the routine within the subcloud layer, which is treated as a decoupled dry boundary layer. The diffusive flux for any quantity ϕ is approximated by a local K closure:

$$\overline{w'\phi'} = -K \frac{\partial \phi}{\partial z}. \quad (A18)$$

For the diffusion of momentum, the eddy diffusivity is set to $K = K_M = \kappa u^* \Phi_{M,0}^{-1} \left(1 - \frac{z}{z_i}\right)^2$ with the von Kármán constant κ , the friction velocity u^* , the stability function for momentum $\Phi_{M,0}$, and the scale height of the boundary layer z_i .

Acknowledgments

We thank Axel Seifert (axel.seifert@dwd.de) for providing the LES data for the RICO case and Lorenzo Tomassini and Stephan de Roode for giving insight into the CONSTRAIN simulations. Moreover, we thank Richard Forbes and Anton Beljaars for fruitful discussions on the study. Moreover, we thank two anonymous reviewers for their constructive comments on the original manuscript.

References

- Arakawa, A., and W. H. Schubert (1974), Interaction of a cumulus cloud ensemble with the large-scale environment, Part I, *J. Atmos. Sci.*, 31(3), 674–701, doi:10.1175/1520-0469(1974)031<0674:IOACCE>2.0.CO;2.
- Baker, L. H., A. C. Rudd, S. Migliorini, and R. N. Bannister (2014), Representation of model error in a convective-scale ensemble prediction system, *Nonlinear Processes Geophys.*, 21(1), 19–39, doi:10.5194/npg-21-19-2014.
- Bechtold, P., N. Semane, P. Lopez, J.-P. Chaboureaud, A. Beljaars, and N. Bormann (2014), Representing equilibrium and nonequilibrium convection in large-scale models, *J. Atmos. Sci.*, 71(2), 734–753, doi:10.1175/JAS-D-13-0163.1.
- Bowler, N. E., A. Arribas, K. R. Mylne, K. B. Robertson, and S. E. Beare (2008), The MORGES short-range ensemble prediction system, *Q. J. R. Meteorol. Soc.*, 134(632), 703–722, doi:10.1002/qj.234.
- Brown, A. (1999), Large-eddy simulation and parametrization of the effects of shear on shallow cumulus convection, *Boundary Layer Meteorol.*, 91(1), 65–80, doi:10.1023/A:1001836612775.
- Brümmer, B., and S. Pohlmann (2000), Wintertime roll and cell convection over Greenland and Barents Sea regions: A climatology, *J. Geophys. Res.*, 105(D12), 15,559–15,566.
- Buizza, R., M. Miller, and T. N. Palmer (1999), Stochastic representation of model uncertainties in the ECMWF ensemble prediction system, *Q. J. R. Meteorol. Soc.*, 125(560), 2887–2908, doi:10.1002/qj.49712556006.
- Carr, M. T., and C. S. Bretherton (2001), Convective momentum transport over the tropical Pacific: Budget estimates, *J. Atmos. Sci.*, 58(13), 1673–1693, doi:10.1175/1520-0469(2001)058<1673:CMTOTT>2.0.CO;2.

- Chelton, D. B., S. K. Esbensen, M. G. Schlax, N. Thum, M. H. Freilich, F. J. Wentz, C. L. Gentemann, M. J. McPhaden, and P. S. Schopf (2001), Observations of coupling between surface wind stress and sea surface temperature in the eastern tropical Pacific, *J. Clim.*, *14*(7), 1479–1498, doi:10.1175/1520-0442(2001)014<1479:OOCBSW>2.0.CO;2.
- Cheng, A., and K.-M. Xu (2014), An explicit representation of vertical momentum transport in a multiscale modeling framework through its 2-D cloud-resolving model component, *J. Geophys. Res. Atmos.*, *119*, 2356–2374, doi:10.1002/2013JD021078.
- Cotton, W., G. Bryan, and S. van den Heever (Eds.) (2011), *Storm and Cloud Dynamics, International Geophysics*, vol. 99, 809 pp., Academic Press, San Diego, Calif.
- de Rooy, W. C., P. Bechtold, K. Fröhlich, C. Hohenegger, H. Jonker, D. Mironov, A. Pier Siebesma, J. Teixeira, and J.-I. Yano (2012), Entrainment and detrainment in cumulus convection: An overview, *Q. J. R. Meteorol. Soc.*, *139*, 1–19, doi:10.1002/qj.1959.
- Dee, D. P., et al. (2011), The ERA-Interim reanalysis: Configuration and performance of the data assimilation system, *Q. J. R. Meteorol. Soc.*, *137*(656), 553–597, doi:10.1002/qj.828.
- ECMWF (2015), *Part IV: Physical Processes*, IFS Documentation, European Centre for Medium-Range Weather Forecasts, England.
- Field, P. R., R. J. Cotton, K. McBeath, A. P. Lock, S. Webster, and R. P. Allan (2014), Improving a convection-permitting model simulation of a cold air outbreak, *Q. J. R. Meteorol. Soc.*, *140*(678), 124–138, doi:10.1002/qj.2116.
- Fu, Q., and K. N. Liou (1993), Parameterization of the radiative properties of cirrus clouds, *J. Atmos. Sci.*, *50*(13), 2008–2025.
- Gregory, D., and M. J. Miller (1989), A numerical study of the parametrization of deep tropical convection, *Q. J. R. Meteorol. Soc.*, *115*(490), 1209–1241, doi:10.1002/qj.49711549003.
- Gregory, D., R. Kershaw, and P. M. Inness (1997), Parametrization of momentum transport by convection: II: Tests in single-column and general circulation models, *Q. J. R. Meteorol. Soc.*, *123*(541), 1153–1183, doi:10.1002/qj.49712354103.
- Grubišić, V., and M. W. Moncrieff (2000), Parameterization of convective momentum transport in highly baroclinic conditions, *J. Atmos. Sci.*, *57*(18), 3035–3049.
- Hogan, T. F., and R. L. Pauley (2007), The impact of convective momentum transport on tropical cyclone track forecasts using the Emanuel cumulus parameterization, *Mon. Weather Rev.*, *135*(4), 1195–1207, doi:10.1175/MWR3365.1.
- Inness, P. M., and D. Gregory (1997), Aspects of the intraseasonal oscillation simulated by the Hadley Centre atmosphere model, *Clim. Dyn.*, *13*(6), 441–458, doi:10.1007/s003820050176.
- Kershaw, R., and D. Gregory (1997), Parametrization of momentum transport by convection. I: Theory and cloud modelling results, *Q. J. R. Meteorol. Soc.*, *123*(541), 1133–1151, doi:10.1002/qj.49712354102.
- Köhler, M., M. Ahlgrimm, and A. Beljaars (2011), Unified treatment of dry convective and stratocumulus-topped boundary layers in the ECMWF model, *Q. J. R. Meteorol. Soc.*, *137*(654), 43–57, doi:10.1002/qj.713.
- LeMone, M. A. (1983), Momentum transport by a line of cumulonimbus, *J. Atmos. Sci.*, *40*(7), 1815–1834.
- Leutbecher, M., and T. N. Palmer (2008), Ensemble forecasting, *J. Comput. Phys.*, *227*(7), 3515–3539, doi:10.1016/j.jcp.2007.02.014.
- Leutbecher, M., S.-J. Lock, P. Ollinaho, S. Lang, G. Balsamo, and P. Bechtold (2016), Stochastic representations of model uncertainties at ECMWF: State of the art and future vision, *Tech. Memo. 785*, ECMWF, European Centre for Medium-Range Weather Forecasts, England.
- Li, D., and E. Bou-Zeid (2011), Coherent structures and the dissimilarity of turbulent transport of momentum and scalars in the unstable atmospheric surface layer, *Boundary Layer Meteorol.*, *140*(2), 243–262, doi:10.1007/s10546-011-9613-5.
- McCabe, A., R. Swinbank, W. Tennant, and A. Lock (2016), Representing model uncertainty in the Met Office convection-permitting ensemble prediction system and its impact on fog forecasting, *Q. J. R. Meteorol. Soc.*, *142*(700), 2897–2910, doi:10.1002/qj.2876.
- Nowlin, W. D., Jr., and C. A. Parker (1974), Effects of a cold-air outbreak on shelf waters of the Gulf of Mexico, *J. Phys. Oceanogr.*, *4*(3), 467–486.
- Ollinaho, P., S.-J. Lock, M. Leutbecher, P. Bechtold, A. Beljaars, A. Bozzo, R. M. Forbes, T. Haiden, R. J. Hogan, and I. Sandu (2016), Towards process-level representation of model uncertainties: Stochastically perturbed parametrisations in the ECMWF ensemble, *Q. J. R. Meteorol. Soc.*, *143*(702), 408–422, doi:10.1002/qj.2931.
- Pincus, R., and B. Stevens (2009), Monte Carlo spectral integration: A consistent approximation for radiative transfer in large eddy simulations, *J. Adv. Model. Earth Syst.*, *1*, 1, doi:10.3894/JAMES.2009.1.1.
- Rauber, R. M., et al. (2007), Rain in shallow cumulus over the ocean: The RICO campaign, *Bull. Am. Meteorol. Soc.*, *88*(12), 1912–1928, doi:10.1175/BAMS-88-12-1912.
- Richter, J. H., and P. J. Rasch (2008), Effects of convective momentum transport on the atmospheric circulation in the community atmosphere model, version 3, *J. Clim.*, *21*(7), 1487–1499, doi:10.1175/2007JCLI1789.1.
- Schlemmer, L., P. Bechtold, I. Sandu, and M. Ahlgrimm (2016), Momentum transport in shallow convection, *Tech. Memo. 781*, ECMWF, European Centre for Medium-Range Weather Forecasts, England.
- Schneider, E. K., and R. S. Lindzen (1976), A discussion of the parameterization of momentum exchange by cumulus convection, *J. Geophys. Res.*, *81*(18), 3158–3160, doi:10.1029/JC081i018p03158.
- Seifert, A., and K. D. Beheng (2001), A double-moment parameterization for simulating autoconversion, accretion and selfcollection, *Atmos. Res.*, *59–60*, 265–281.
- Seifert, A., and K. D. Beheng (2006), A two-moment cloud microphysics parameterization for mixed-phase clouds: Part 1: Model description, *Meteorol. Atmos. Phys.*, *92*, 45–66.
- Seifert, A., T. Heus, R. Pincus, and B. Stevens (2015), Large-eddy simulation of the transient and near-equilibrium behavior of precipitating shallow convection, *J. Adv. Model. Earth Syst.*, *7*, 1918–1937, doi:10.1002/2015MS000489.
- Shutts, G. J., and T. N. Palmer (2007), Convective forcing fluctuations in a cloud-resolving model: Relevance to the stochastic parameterization problem, *J. Clim.*, *20*(2), 187–202, doi:10.1175/JCLI3954.1.
- Stevens, B., and A. Seifert (2008), Understanding macrophysical outcomes of microphysical choices in simulations of shallow cumulus convection, *J. Meteorol. Soc. Jpn.*, *86*, 143–162.
- Stevens, B., et al. (2005), Evaluation of large-eddy simulations via observations of nocturnal marine stratocumulus, *Mon. Weather Rev.*, *133*(6), 1443–1462.
- Tiedtke, M. (1989), A comprehensive mass flux scheme for cumulus parameterization in large-scale models, *Mon. Weather Rev.*, *117*, 1779–1800.
- Tomassini, L., P. R. Field, R. Honnert, S. Malardel, R. McTaggart-Cowan, K. Saitou, A. T. Noda, and A. Seifert (2017), The “Grey Zone” cold air outbreak global model intercomparison: A cross-evaluation using large-eddy simulations, *J. Adv. Model. Earth Syst.*, *9*, 39–64, doi:10.1002/2016MS000822.
- Tulich, S. N. (2015), A strategy for representing the effects of convective momentum transport in multiscale models: Evaluation using a new superparameterized version of the Weather Research and Forecast model (SP-WRF), *J. Adv. Model. Earth Syst.*, *7*, 938–962, doi:10.1002/2014MS000417.

- Tung, W., and M. Yanai (2002a), Convective momentum transport observed during the TOGA COARE IOP: Part I: General features, *J. Atmos. Sci.*, *59*(11), 1857–1871.
- Tung, W., and M. Yanai (2002b), Convective momentum transport observed during the TOGA COARE IOP: Part II: Case studies, *J. Atmos. Sci.*, *59*(17), 2535–2549.
- vanZanten, M. C., et al. (2011), Controls on precipitation and cloudiness in simulations of trade-wind cumulus as observed during RICO, *J. Adv. Model. Earth Syst.*, *3*, M06001, doi:10.1029/2011MS000056.
- Wu, X., and M. Yanai (1994), Effects of vertical wind shear on the cumulus transport of momentum: Observations and parameterization, *J. Atmos. Sci.*, *51*(12), 1640–1660.
- Wu, X., L. Deng, X. Song, and G. J. Zhang (2007), Coupling of convective momentum transport with convective heating in global climate simulations, *J. Atmos. Sci.*, *64*(4), 1334–1349, doi:10.1175/JAS3894.1.
- Zhang, G. J., and H.-R. Cho (1991), Parameterization of the vertical transport of momentum by cumulus clouds: Part I: Theory, *J. Atmos. Sci.*, *48*(12), 1483–1492, doi:10.1175/1520-0469(1991)048<1483:POTVTO>2.0.CO;2.
- Zhang, G. J., and N. A. McFarlane (1995), Role of convective scale momentum transport in climate simulation, *J. Geophys. Res.*, *100*(D1), 1417–1426, doi:10.1029/94JD02519.
- Zhang, G. J., and X. Wu (2003), Convective momentum transport and perturbation pressure field from a cloud-resolving model simulation, *J. Atmos. Sci.*, *60*(9), 1120–1139.
- Zhu, P. (2015), On the mass-flux representation of vertical transport in moist convection, *J. Atmos. Sci.*, *72*(12), 4445–4468.